Spectroscopic Investigation of CdS Quantum Dots and Fe^{2+}:ZnSe

by

Ahmet Koray Erdamar

A Thesis Submitted to the
Graduate School of Sciences and Engineering
in Partial Fulfillment of the Requirements for
the Degree of

Master of Science

in

Physics

Koç University

August 2007

Koç University

Graduate School of Sciences and Engineering

This is to certify that I have examined this copy of a master's thesis by

Ahmet Koray Erdamar

and have found that it is complete and satisfactory in all respects,
and that any and all revisions required by the final
examining committee have been made.

Committee Members:

_____

Alphan Sennaroğlu, Ph. D. (Advisor)

_____

H. Funda Yağcı Acar, Ph. D.

_____

Alper Kiraz, Ph. D.

Date: _____

Canım Aileme...

ABSTRACT

In this work, spectroscopic properties of CdS quantum dots and Fe^{2+}:ZnSe crystals were investigated. In the first part of the thesis, visible luminescence characteristics of CdS quantum dots were studied. Poly (acrylic acid) (PAA) coated CdS quantum dots were prepared in aqueous solutions. Influence of reaction pH, PAA molecular weight (2100 and 5100 g/mol), and COOH/Cd ratio on the particle size, colloidal stability, and photoluminescence (PL) efficiency were investigated. These quantum dots have an absorption band below 508 nm. Nanoparticle sizes were determined from the absorption onset wavelength by using the Brus equation. PL studies of the samples were performed at the excitation wavelength of 355 nm. Luminescence quantum yields were measured with respect to Rhodamine B. Results show that there is a critical COOH/Cd ratio (1.5-2) that gives the highest quantum yield (17%). This critical value corresponds to smaller crystal sizes (3.7-4.1 nm). Moreover, CdS nanoparticles prepared at pH 7.5 exhibited higher quantum yields than those prepared at 5.5.

In the second part of the thesis, absorption saturation characteristics of Fe^{2+}:ZnSe samples are discussed. In these experiments, a tunable Cr^{2+}:ZnSe laser producing 10-30 ns pulses was used as the pump source. The repetition rate was 1 kHz. Saturation measurements were performed at two different wavelengths (2645 and 2730 nm) by employing the z-scan and power transmission methods. The average value of the absorption cross section (σ_a) and normalized-excited state absorption strength (f_p) were determined to be 1.73×10^{-19} cm^2 and 0.23 2645 nm, respectively. At the wavelength of 2730 nm, the respective values were 2.47×10^{-19} cm^2 and 0.17. Attempt was made to measure the fluorescence lifetimes of single-crystal and polycrystalline Fe^{2+}:ZnSe at room temperature and at cryogenic temperatures. However, sufficient fluorescence signal could not be obtained. The design of the cryogenic system used for attaining low temperatures is also described.

ÖZET

Bu çalışmada, CdS kuvantum noktalarının ve Fe^{2+}:ZnSe kristallerinin spektroskopik özellikleri araştırıldı. Tezin ilk bölümünde CdS kuvantum noktalarının görünür bölgedeki ışıma özellikleri incelendi. Poly(acrylic asit) (PAA) ile kaplanmış olan CdS quvantum noktaları sulu çözelti içerisinde hazırlandı. Reaksiyon pH değerinin, PAA molekül ağırlığının (2100 ve 5100 g/mol) ve COOH/Cd oranının parçacık büyüklüğüne ve ışıma verimine olan etkileri araştırıldı. Deneylerde kullanılan kuvantum noktalarının soğurma bantları 508 nm altındadır. Nanoparçacıkların boyutları soğurma spektrumu kullanılarak Brus denklemi ile belirlendi. 355 nm dalga boyundaki pompa kullanılarak örneklerin ışıma ölçümleri yapıldı. Örneklerin ışıma verimleri Rhodamine B referansına göre belirlendi. Deneylerin sonucunda en yüksek ışıma veriminin (17%) kritik COOH/Cd oranında (1.5-2) elde edildiği görüldü. Bu kritik oranın aynı zamanda daha küçük kristal boyutları elde edebilmek için de uyumlu olduğu belirlendi. Bununla birlikte, pH 7.5 değerinde hazırlanmış olan CdS nanoparçacıklarının, pH 5.5 değerinde hazırlanmış olanlara göre daha yüksek kuvantum verimlerinin olduğu gözlemlendi.

Tezin ikinci bölümünde Fe^{2+}:ZnSe örneklerinin doyabilen soğurma özellikleri incelendi. Bu deneylerde dalga boyu ayarlanabilir, darbe tekrar sıklığı 1kHz olan ve 10-30 ns darbe genişliğine sahip Cr^{2+}:ZnSe laseri pompa olarak kullanıldı. Doygunluk ölçümleri iki farklı dalga boyunda (2645 ve 2730 nm) z-taramalı ve güç geçirgenliği metotlarıyla yapıldı. 2645 nm pompa gücündeki ölçümler için ortalama temel düzey ve uyarılmış düzey soğurma arakesit değerleri 1.73×10^{-19} cm^2 ve 0.23 olarak belirlendi. 2730 nm pompa gücündeki değerleri ise 2.47×10^{-19} cm^2 ve 0.17 olarak bulundu. Yaşam süresi ölçümleri denemeleri tekli ve çoklu kristal yapısına sahip Fe^{2+}:ZnSe örnekleriyle oda sıcaklığında ve düşük sıcaklıklarda denendi. Fakat yeterli ışıma sinyali elde edilemedi. Düşük sıcaklıklarda ölçüm yapmak için tasarlanan soğutma sisteminin yapımı da tezde anlatılmıştır.

ACKNOWLEDGEMENTS

This thesis will be on “Spectroscopic Investigation of CdS Quantum Dots and Fe^{2+}:ZnSe”. This study is the result of my work as a graduate research assistant at the Laser Research Laboratory (LRL) of Koc University (KU) in the years 2005-2007. It would have been impossible without the help of many people. As my work for a MS degree at Koc University ends, I would like to thank all the people that made this work possible.

First of all, I would like to thank my research advisor Dr. Alphan Sennaroğlu for his continuous guidance and generous supports throughout my study. I would also like to thank Adnan Kurt for his time, constant involvement with my research at LRL. I would like to express my deepest gratitude to Dr. Alphan Sennaroğlu and Adnan Kurt for their contributions, and detailed comments. My interaction with them has provided me a great opportunity to gain experience in experimental research, learning a lot from their numerous technical skills.

I would like to thank Dr. Havva Funda Yağcı Acar, Serdar Çelebi and all members of Polymer and Nanomaterials Research Group for their collaboration and contributions on “Characterization of CdS Quantum Dots”. Especially, this project would not have been possible without the continuing support and excitement of Dr. Havva Funda Yağcı Acar.

I would also like to thank Dr. Alper Kiraz for taking his valuable time to serve on my thesis committee.

I would especially like to thank Ümit Demirbaş, who is the former member of KU LRL, for his time and for sharing his experience. I would also gratefully acknowledge Hamit Kalaycıoğlu and Hüseyin Çankaya for their advices, comments and continuing supports during the experiments. I would like to thank Reyhane Kılcı, Ahmet Faruk Çoşkun and Natali Çizmeciyan for their friendship and supports during my MS study.

I would gratefully acknowledge my best friend Serhat Tozburun for his endless friendship, all his support and generous help for the past 11 years that include high-school, undergraduate, and graduate education life.

The primary support for my studies was provided by KU and TÜBİTAK (The Scientific and Technical Research Council of Turkey). I am grateful for their support without which this work would not have been possible.

I wish to thank Z. Ceyda Beyazyıldırım for her deep love, endless support and tolerance during my studies.

Finally, I am grateful to my family, for their continuing support, love and patience during my entire time at KU. It is to them, I wish to dedicate this thesis.

TABLE OF CONTENTS

LIST OF TABLES

LIST OF FIGURES

NOMENCLATURE

a	an integer
a_B	Bohr radius
A	cross sectional area
Abs	absorption
c	speed of light
C	a constant
dz	thickness
D	a constant
e	electron charge
E	energy eigenvalue
E_e	energy eigenvalue for electron
E_h	energy eigenvalue for hole
E_{gap}	band gap energy of the bulk material
E^*	band gap energy of the nanocrystal
$\overline{E}_p$	integrated pump pulse energy per unit area
E_{sa}	absorption saturation energy
f_p	normalized excited-state absorption cross section
h	Planck constant
I	PL intensity
I_{calib}	calibrated PL intensity
I_p	pump laser intensity
$j_l(\mathrm{x})$	spherical Bessel function of order l
$\hat{L}^2$	angular momentum operator
m	mass of particle
m_e	effective mass of electron
m_h	effective mass of hole

m_r	reduced mass
m_0	mass of electron
M^2	a parameter for quantifying the beam quality of laser beams
n_l(x)	Neumann functions of order l
n_{ZnSe}	index of refraction of ZnSe crystal
N_{Fe}	iron ion concentration
N_g	population density of ions in the ground-state
N_2	population density of ions in the second state
$R_{n,l}(r)$	radial part of the wave function
R	radius
t	time
u_p	electromagnetic energy density
$V(r)$	position-dependent potential energy
v_g	group velocity of the electromagnetic wave
v_p	pump laser frequency
$w_p(z)$	position-dependent spot size function
w_{p0}	pump beam waist
$Y_l^m(\theta,\phi)$	spherical harmonics
z_{fp}	beam waist location
z_{Rp}	Rayleigh range
τ_f	fluorescence lifetime
λ_{nm}	onset wavelength
λ_p	pump laser wavelength
ΔE	band gap differences
$\sigma_a(\lambda)$	absorption cross section at λ
σ_{esa}	excited-state absorption cross section
$\alpha_{p0}(\lambda)$	absorption coefficient at λ
Φ_p	normalized distribution function

η	relative luminescence quantum yield
φ	diameter
$\psi(r)$	wave function
∇	del operator
ε	dielectric constant for the bulk semiconductor
ε_0	vacuum permittivity
$\|g\rangle$	ground-state energy level
$\|1\rangle$	first state energy level
$\|2\rangle$	second state energy level
$\|3\rangle$	upper energy level
$\|4\rangle$	higher energy level

Chapter 1

Introduction

1.1 Overview of Quantum Dots

Semiconductor nanoparticles, also known as quantum dots (QD), have been investigated over the past decades due to their favorable optical and electronic properties. A sample of the bulk material does not have the same properties as that in nanoparticle form. Due to the confinement of the electron in all directions, quantum dots have size-tunable narrow bandwidth photoluminescence [1]. In the quantum dots, all band properties of the bulk semiconductor materials are still applicable. As an added advantage, quantum dots have variable band gap that depends on size. As the size of the crystal decreases, the band gap value of the quantum dot increases [2]. Therefore, the required energy for absorption increases by decreasing the size of the quantum dots. This result gives blue shift in both absorption and emission spectra of the quantum dots. Thus, the output wavelength of the quantum dot can be tuned. These optical properties have resulted in many applications of QDs in science and industry, such as LEDs, lasers, solar cells, sensors, biological labeling, and medical imaging [3-7].

Compound semiconductors are composed of elements from the groups of II-VI, III-V, or IV-VI. CdS, CdSe, and CdTe are examples of II-VI semiconductor nanocrystals that have been studied widely due to their emission in the visible spectrum, while group IV-VI quantum dots, such as PbS, PbSe, and PbTe emit in the infrared region [8]. Controlling the size of quantum dots is very important due to its unique properties. The control mechanism is generally performed by chemical methods. Nanoparticles are usually prepared as core-shell structures. Organic shell is adsorbed on the surface of the crystal to control the particle growth by surface passivization [9]. In quantum dots,

surface defects limit the luminescence efficiency. Therefore, effective surface passivization is important for the optical properties of the quantum dots [10]. In order to prepare the desired quantum dots, surfactant types and synthesis conditions are crucial.

In this work, in collaboration with Yagci and Celebi, we investigated the spectroscopic properties of Poly(acrylic acid) (PAA) coated CdS quantum dots. To our knowledge, this is the first study in the literature that is investigating the effect of PAA molecular weight and amount on particle properties [11]. In Chapter 2, we present the theoretical analysis of quantum dots, and discuss the Brus equation [2] which is widely used in the determination of the size of the quantum dots. In Chapter 3, we characterize the PAA coated CdS quantum dots with respect to their particle properties, such as crystal size, photoluminescence emission intensity, and quantum yield.

1.2 Overview of the Spectroscopy of Fe^{2+}:ZnSe

The second part of the thesis investigates the spectroscopic characteristics of potentially important tunable solid-state laser material. Tunable solid state lasers have applications in many fields, such as biomedical imaging, remote sensing, military countermeasures, and the detection of organic and inorganic compounds [12, 13]. In the last four decades, spectroscopic investigation of transition metal (TM) ion-doped II-VI semiconductor crystals (chalcogenides) showed that these materials have strong emission bands in the mid-infrared spectral range from 2 to 5 μm [14-18]. In 1996, DeLoach et al. investigated the spectroscopic properties of Cr^{2+}, Co^{2+}, Ni^{2+}, and Fe^{2+} doped chalcogenide hosts of ZnS, ZnSe, and ZnTe [19]. They observed high gain, room-temperature lasing in Cr^{2+}:ZnSe [19, 20]. The success of the Cr^{2+}:ZnSe laser initiated further research on the investigation of other TM ion doped chalcogenides crystals.

The lack of tunable 3-5 μm solid state lasers stimulated interest in Fe ion doped II-VI crystals, especially ZnSe. Undoped ZnSe crystal is transparent in the spectral range from 0.5 to 22 μm [21]. Doping Fe ions into the ZnSe crystal has two important effects. First effect is the difference in the absorption edge wavelength. The short wavelength absorption edge for pure ZnSe is about 470 nm, which corresponds to the band gap

energy of the crystal [22]. However, iron-doped ZnSe crystals have absorption edge in the longer wavelength around 520 nm [23]. The diffused Fe ions take the place of Zn in the host material. Generally, they take part in the form of Fe^{2+} in the crystal lattice. Transition metal ions might also be in other forms such as Fe^{1+}, or Fe^{3+} in the chalcogenide crystals. Therefore, the difference in the short wavelength absorption edge is due to transitions between the different charge states of Fe ions. Second, Fe-doped ZnSe crystals have a strong and wide absorption band with a maximum around 3 μm. Further more, when excited around 3μm, Fe^{2+}:ZnSe emits in the 3-5 μm range and can be used as a tunable laser medium. However, mid-infrared transitions in Fe^{2+}:ZnSe crystal suffer from multi-phonon quenching at room temperature [19]. Therefore, the first successful laser studies in Fe^{2+}:ZnSe crystal were performed at low temperatures [13, 24-26]. The room temperature lasing was obtained in later studies [27, 28]. Up to now, the overall tuning range demonstrated with the Fe^{2+}:ZnSe laser is 3.77-5.05 μm [28].

Besides the laser application of Fe^{2+}:ZnSe crystal, it can also be used as a saturable absorber for lasers working around 3 μm [29, 30]. In this work, saturation analysis of Fe^{2+}:ZnSe was performed at two different wavelengths and with two different methods. The theoretical model and experiments are discussed in Chapter 4. Chapter 5 describes the attempts aimed to making lifetime measurements and lasing of Fe^{2+}:ZnSe crystal at both low and room temperature. In order to perform experiments at low temperature, a cryogenic system was designed and constructed. This is also discussed in Chapter 5.

Chapter 2

Theoretical Analysis of Quantum Dots

In this chapter, we first provide background about quantum dots and discuss how they differ from bulk semiconductor materials. In section 2.2 quantum mechanical models of quantum dots are presented. Finally, we introduce the effective mass approximation method and discuss the Brus equation which is widely used in the determination of the size of quantum dots.

2.1 Introduction

The development in the fabrication of low-dimensional semiconductor structures made it possible to reduce the three dimensional bulk materials, to quasi-two, quasi-one, and even to quasi-zero dimensional systems. Invention of low dimensional structures began in 1970s by Esaki and Tsu [31]. These two dimensional structures were called quantum wells, and were applied to electronic and optoelectronic applications successfully. This success initiated a lot of new studies in this field. As a result of these studies and rapid change in the technology; at the beginning in 1980s, one dimensional structures known as “quantum wires” emerged [31]. In these structures, the electron is confined in one or more dimensions. In a quantum well, the electron is confined in one direction, whereas it is confined in two dimensions inside a quantum wire. In a quantum dot, on the other hand, the electron is trapped in three dimensions. Quantum dot systems are similar to atoms due to the confinement in all dimensions. Because of the similarity with atoms, they are also called artificial atoms. Quantum dots are a unique class of semiconductors and exhibit size-dependent behavior. Because their sizes are in the nanometer scale, they are also called nanocrystals or nanoparticles.

Nanoparticles have different and advanced properties such as tunable band gap, discrete energy levels and size dependent optical properties when they are compared with bulk materials. In bulk form, energy levels are very closely spaced and form continuum of allowed levels known as energy bands. This is a typical property of bulk semiconductor crystals which have fixed and unchangeable band gap because of this reason. Band gap is the energy difference between the conduction and valance bands of material. Energy difference is usually on the order of an electronvolt (eV) for semiconductors. In bulk semiconductor materials, majority of electrons fill the valance band, while only a small number of electrons occupy the conduction band. In order to fill the conduction band, electrons in the valance band must cross the band gap. This process cannot happen spontaneously. Electrons need additional energy to jump to higher energy levels. Stimulus effects such as a voltage bias, heat, or light can provide enough energy to electron to cross the band gap. In order to excite electrons from valance band to conduction band, absorbed energy must be equal or larger than the band gap energy of bulk semiconductor [8, 32]. Excited electrons leave holes behind in the valance band, and they emit electromagnetic radiation while they fall back from conduction band to lower energy levels in the valance band [8]. In other words, electrons move from one edge of band gap to the other. Emitted wavelength corresponds to the band gap of the bulk material. Because of the fixed band gap in bulk semiconductor, emitted radiation has nearly a fixed wavelength.

At this point, quantum dots differ from bulk semiconductors. In quantum dots, all concepts of semiconductors such as conduction band and valance band are still applicable. The excited electron in the conduction band and the hole in the valance band can form a bound. This electron-hole pair is called exciton and is shown in Figure 2.1 [8, 33].

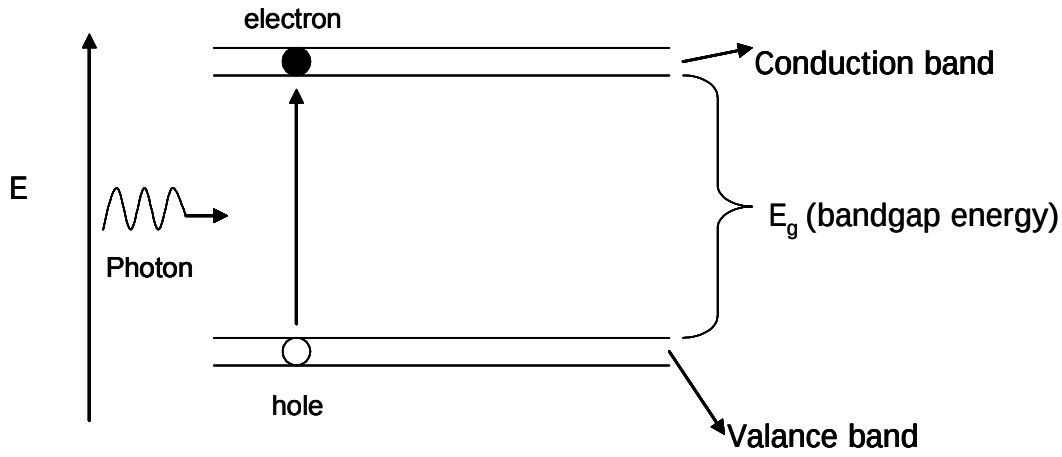

Figure 2.1: Generation of an exciton.

The distance between the electron in the conduction band and the hole in the valance band is called exciton Bohr radius. This is different for each material. In bulk material, the size of semiconductor material is larger than the exciton Bohr radius [8]. When the size of semiconductors crystals becomes small enough and comparable to exciton Bohr radius, the energy levels of the material become discrete. Here 'discrete' means that there is small and finite energy separation between the energy levels. Having discrete energy levels result in a tunable band gap. Addition or subtraction of atoms to the quantum dot causes a change in the band gap. Such addition or subtraction does not affect the bulk material because of the latter's larger size. Ability to change the band gap of quantum dots leads to light emission at different wavelengths [34]. Therefore, by controlling the size of the dot, output wavelength can be estimated precisely. In order to determine the size of quantum dot from absorption data, Brus proposed a quantum mechanical model based on the effective mass approximation [2]. In what follows, we will systematically review the basic quantum mechanical analysis of potential wells and discuss the details of the Brus model.

2.2 Theoretical Models

2.2.1 One-Dimensional Potential Well

One-dimensional potential well problem is the simplest confinement potential problem in quantum mechanics. Before treating the quantum dot systems, it is necessary to understand the consequences of one-dimensional particle in an infinite potential well.

The time-independent Schrödinger equation must be solved for the motion of a single electron in an infinite potential well [35]:

$$\left\{-\frac{\hbar^2}{2m}\nabla^2 + V(r)\right\}\psi(r) = E\psi(r)\,. \tag{2.1}$$

Here, $\psi(r)$ is the wave function, ∇ is the del operator, and E is the energy eigenvalue. V(r) represents the position-dependent potential energy of the system. Assuming that we have a one-dimensional potential which varies along z-axis, the Schrödinger equation becomes

$$-\frac{\hbar^2}{2m}\frac{\partial^2}{\partial z^2}\psi(z) + V(z)\psi(z) = E\psi(z). \tag{2.2}$$

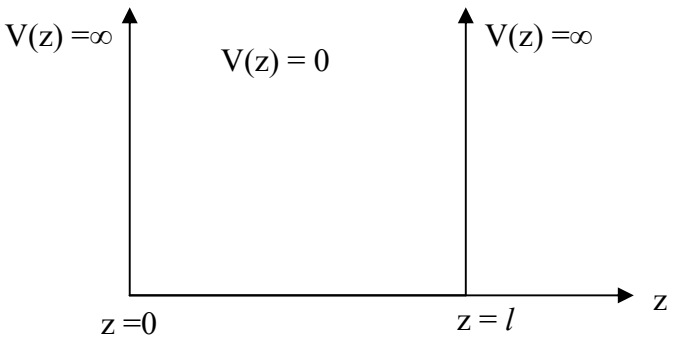

Figure 2.2: One dimensionl infinite potential well.

Outside of the well, the potential is infinite and inside of the well it is zero. Only $\psi(z)$ is non-zero inside the well. The Schrödinger equation simplifies to

$$-\frac{\hbar^2}{2m}\frac{\partial^2}{\partial z^2}\psi(z) = E\psi(z), \tag{2.3}$$

which has a solution of the form $\psi(z) = C\sin kz + D\cos kz$. The corresponding energy eigenvalues are

$$E = \frac{\hbar^2 k^2}{2m}. \tag{2.4}$$

When the boundary conditions are applied to the function $\psi(z)$, cosine term disappears since $\psi = 0$ at $z = 0$. The wave function becomes $\psi(z) = C\sin kz$. ψ should also be zero at $z = l$, giving

$$k = \frac{\pi a}{l}, \tag{2.5}$$

where *a* is an integer [33]. When this equation is substituted into the equation 2.4, the energy for different states can be obtained from

$$E = \frac{\hbar^2 \pi^2 a^2}{2ml^2}. \tag{2.6}$$

Next, we investigate the 3-dimensional potential well with spherical symmetry in spherical coordinates.

2.2.2 Spherical Potential Well

Due to the spherical symmetry of the quantum dot, the energy eigenvalues of the quantum dot can be more easily obtained in spherical coordinates. We consider a particle of mass *m* confined to the interior of a spherical well.

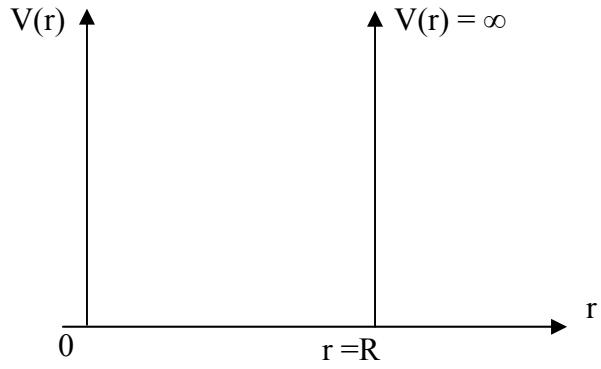

Figure 2.3: Infinite spherical potential well.

In an infinite potential well, the potential satisfier: V(r) = 0 for r<R, and V(r) = ∞ for r>R. By using the method of separation of variable, $\psi(r,\theta,\phi)$ can be written as a product in the form:

$$\psi_{n,l,m}(r,\theta,\phi) = R_{n,l}(r)\, Y_l^m(\theta,\phi) \ , \tag{2.7}$$

where $Y_l^m(\theta,\phi)$ are spherical harmonics, $R_{n,l}(r)$ is radial part of the wave function and *n, l, m* are quantum numbers [36, 37]. The time independent Schrödinger equation for a free particle in spherical coordinates can be written as

$$\left[\frac{1}{2m}\left(\hat{p}_r{}^2 + \frac{\hat{L}^2}{r^2}\right) + V(r)\right]\psi_{n,l,m} = E_{n,l}\psi_{n,l,m}\,, \tag{2.8}$$

where $\frac{\hat{p}_r^{\,2}}{2m}$ is the radial kinetic energy operator, and $\hat{L}^2$ is the angular momentum operator [37]. The first term is a function of *r*, and $\hat{L}^2$ is a function of only the angle variables (θ,ϕ). Substituting equation 2.7 into equation 2.8 gives

$$\left\{-\frac{\hbar^2}{2m}\left[\frac{1}{r}\frac{d^2}{dr^2}r-\frac{L^2}{\hbar^2 r^2}\right]+V(r)\right\}R_{n,l}(r)=E_{n,l}R_{n,l}(r). \tag{2.9}$$

Substituting L^2 into the equation 2.9 gives us the final form of "Radial Schrödinger Equation" as

$$\left[-\frac{\hbar^2}{2m}\frac{1}{r}\frac{d^2}{dr^2}r+\frac{\hbar^2 l(l+1)}{2mr^2}+V(r)\right]R_{n,l}(r)=E_{n,l}R_{n,l}(r). \tag{2.10}$$

Outside the well the wave equation is zero. Inside the well radial equation becomes

$$\frac{1}{r}\frac{d^2}{dr^2}\left[rR_{n,l}(r)\right]+\left[k^2-\frac{l(l+1)}{r^2}\right]R_{n,l}(r)=0. \tag{2.11}$$

where $k^2=\frac{2mE}{\hbar^2}$. With the substitution $U(r)\equiv R_{n,l}(r)r$ [36] equation 2.11 becomes

$$\frac{d^2U(r)}{dr^2}+\left(k^2-\frac{l(l+1)}{r^2}\right)U(r)=0. \tag{2.12}$$

For the case $l=0$ this equation yields same results with one dimensional infinite potential well. For an arbitrary integer *l* the solution to equation 2.12 is not so familiar.

With the substitution of $x \equiv kr$ into the equation 2.11 we get spherical Bessel differential equation as [37]

$$\frac{d^2}{dx^2}R(x)+\frac{2}{x}\frac{dR(x)}{dx}+\left[1-\frac{l(l+1)}{x^2}\right]R(x)=0. \tag{2.13}$$

R has two linearly independent solutions. They are called spherical Bessel and Neumann functions of order l and are denoted by the symbols $j_l(x)$ and $n_l(x)$, respectively. The first few values of these functions are [37]

$$\begin{aligned} j_0(x) &= \frac{\sin x}{x} & n_0(x) &= \frac{\cos x}{x} \\ j_1(x) &= \frac{\sin x}{x}-\frac{\cos x}{x} & n_1(x) &= -\frac{\cos x}{x}-\frac{\sin x}{x} \\ j_2(x) &= \left(\frac{3}{x^3}-\frac{1}{x}\right)\sin x-\frac{3}{x^2}\cos x & n_2(x) &= -\left(\frac{3}{x^3}-\frac{1}{x}\right)\cos x-\frac{3}{x^2}\sin x. \end{aligned} \tag{2.14}$$

From equation 2.14 general formulas can be obtained for these functions as,

$$j_l(x)=(-x)^l\left(\frac{1}{x}\frac{d}{dx}\right)^l j_0(x) \qquad n_l(\mathrm{x})=(-x)^l\left(\frac{1}{\mathrm{x}}\frac{d}{dx}\right)^l n_0(x). \tag{2.15}$$

With this manner, for arbitrary l values the solution of equation 2.12 becomes

$$U(r)=Crj_l(kr)+Drn_l(kr). \tag{2.16}$$

The Bessel functions are finite and regular at the origin, but the Neumann functions are irregular at the origin. Therefore, we set the value of $D=0$, and equation 2.16 becomes

$$U(r) = Crj_l(kr) \qquad \text{and} \qquad R_{n,l}(r) = Cj_l(kr). \tag{2.17}$$

For boundary conditions r = R, radial equation becomes $R_{n,l}(r) = 0$. So we can write Bessel function as

$$j_l(kR) = 0. \tag{2.18}$$

When we return to the notation $x \equiv kr$, equation 2.18 becomes

$$j_l(x_{ln}) = 0, \tag{2.19}$$

where x_{ln} is n^{th} zero of l^{th} order spherical Bessel function. The following table gives the first number of zeros of $j_l(x)$ [37].

(l,n)	(0,1)	(1,1)	(2,1)	(0,2)	(3,1)	(1,2)	(4,1)
x_{ln}	π	4.99	5.76	2π	6.99	7.73	8.18

Table 2.1: List of first number of zeros of $j_l(x)$

Eigen functions and eigenenergies for the spherical well are then given by

$$\psi_{n,l,m}(r,\theta,\phi) = C_{nl} j_l\left(\frac{x_{ln} r}{R}\right) Y_l^m(\theta,\phi) \ , \tag{2.20}$$

$$E_{nl} = \frac{\hbar^2 x_{ln}^2}{2mR^2}. \tag{2.21}$$

When the ground state value of $x_{01} = \pi$ is substituted into equation 2.21, ground-state eigenenergies for spherical well can be expressed as

$$E_{nl} = \frac{\hbar^2 \pi^2}{2mR^2}. \tag{2.22}$$

In order to understand the size dependent band gap, different theoretical approaches have been adopted. One of these approaches is effective mass approximation (EMA) that relies on infinite well problem [2, 38, 39].

2.3 Effective Mass Approximation Method

Band gap structure of semiconductor and formation of exciton are discussed in section 2.1. The binding energy and the orbital radius of the exciton can be described in the Bohr Theory. The two-body nature of the system should also be takes into account. The electron mass becomes the reduced mass of the electron-hole pair, and is given by

$$\frac{1}{m_r} = \frac{1}{m_e} + \frac{1}{m_h}, \tag{2.23}$$

where m_e is the effective mass of electron and m_h is the effective mass of the hole [8]. The distance between the electron and the hole is called the exciton Bohr radius. It is obtained by using reduced mass in the well known Bohr Radius expression. For a bulk semiconductor, it is given by,

$$a_B = \frac{\varepsilon \hbar^2}{m_r e^2}, \tag{2.24}$$

where ε is the dielectric constant for the bulk semiconductor and e is the electron charge [8].

Effective mass varies in different materials. It is also different for electrons and holes in the same material [40]. That is the reason why exciton Bohr radius varies for

different materials. Quantum confinement can be explained in terms of the Bohr radius. When the radius R of the nanocrystal is smaller than the exciton Bohr radius, strong confinement regime occurs [35, 41]. In this configuration, the Coulomb interaction becomes important and reduce the transition energy [41].

In order to evaluate the transition energy, Brus solved the Schrödinger equation for the electron-hole states,

$$\left[\frac{-\hbar^2}{2m_e}\nabla_e^2+\frac{-\hbar^2}{2m_h}\nabla_h^2+V_o(r)\right]\psi(r)=E\psi(r) \tag{2.25}$$

which is also known as the hydrogenic Hamiltonian [2]. The solution gives the energy values for electron and hole separately where,

$$E_e=E_g+\frac{\hbar^2\pi^2}{2m_eR^2}, \qquad E_h=\frac{\hbar^2\pi^2}{2m_hR^2}\cdot \tag{2.26}$$

The transition energy can be expressed as [2, 32, 42]

$$E^*=E_{gap}+\frac{\hbar^2\pi^2}{2R^2}\left[\frac{1}{m_e}+\frac{1}{m_h}\right]-\frac{1.8e^2}{4\pi\varepsilon R}+\text{higher order correction.} \tag{2.27}$$

E_g is the bulk crystal band gap value while E^* is the band gap value of the nanoparticles. The second term is the quantum energy of localization for both electron and hole. The third term is due to Coulomb attraction. ε is dielectric constant for the bulk material which is $5.7\varepsilon_0$ for CdS quantum dots [2]. R is the radius of the nanocrystals. Higher-order terms are typically neglected. For large band gap materials, the Coulomb term is

important and must be added to the calculation. When the band gap is small, Coulomb term is not as important in the calculations [42].

2.3.1 Application of Brus Equation to CdS Nanoparticles

From equation 2.27, the radius R of the nanoparticles (R) can be calculated. Neglecting the higher-order terms, equation 2.27 can be written in the form

$$\Delta E = \frac{\hbar^2 \pi^2}{2R^2}\left[\frac{1}{m_e} + \frac{1}{m_h}\right] - \frac{1.8e^2}{4\pi\varepsilon R}. \tag{2.28}$$

In order to analyze this equation easily, its simplified form can be written as,

$$X = Y - Z \tag{2.29}$$

where X, Y and Z define the band gap differences, quantum energy of localization for both electron and hole and Coulomb attraction, respectively. Determination of band gap differences (X) is straight forward and easy method. Band gap differences is given by the expression,

$$\Delta E = E^* - E_{gap} \ . \tag{2.30}$$

It gives us the band gap shift with respect to the bulk value. E_{gap} is the band gap of the bulk material. This value is 2.41 eV for CdS [43]. E^* is the band gap value of the nanocrystal. It can be obtained by the absorption analysis of the sample [44]. Figure 2.4 shows absorption analysis of CdS sample with Poly(acrylic acid)2K (PAA), COOH/Cd ratio of 1.5 and with pH 5.5. In order to find the onset wavelength, firstly, an arbitrary linear line is drawn from the start of absorption onset. Then, a reference line is drawn

that starts before the absorption onset. The intersection of these two lines is absorption edge and gives us absorption onset wavelength.

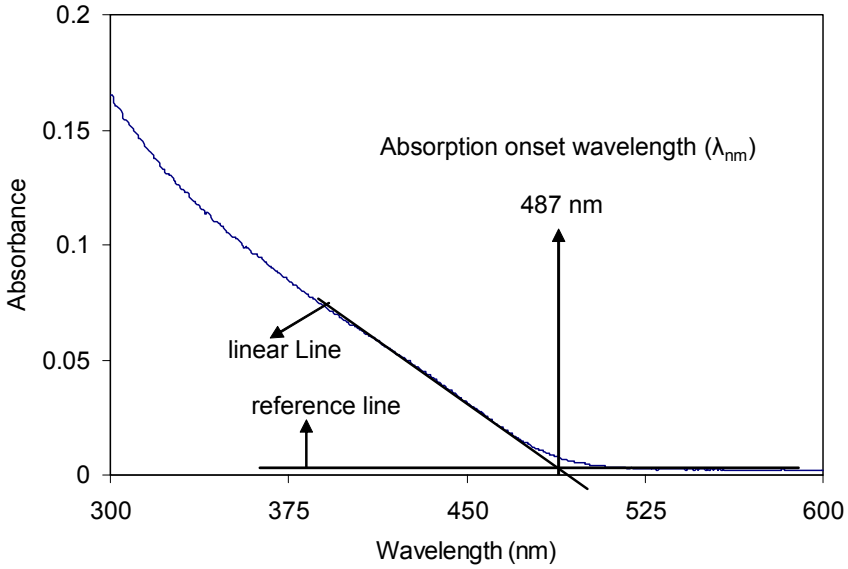

Figure 2.4: Absorbance of CdS nanoparticles, showing the absorption onset wavelength.

The onset point in the absorption analysis graph is the critical point for calculating the band gap energy of nanoparticles. The well known formula (Planck's relation) for the energy is

$$E^* = \frac{h\,c}{\lambda_{nm}} = \frac{6.626\times10^{-34}\left[J.s\right]\times(2.998\times10^{8}\left[m/s\right]}{\lambda(nm)} \approx \frac{1240eV(nm)}{\lambda(nm)}, \qquad (2.31)$$

where c is the speed of light, h is Planck constant and λ_{nm} is the onset wavelength (in nanometers) of the absorption band. In Figure 2.4, when the onset wavelength is 487 nm, obtained E^* is 2.55 eV from equation 2.31. This value is shifted when it is compared with the bulk material band gap energy. It is the effect of the size quantization in the sample. Reduction in the size causes a shift in the band gap of the bulk sample. Equation 2.30 takes the form,

$$\Delta E \cong \frac{1240[eV - nm]}{\lambda(nm)} - 2.41eV = X \ . \tag{2.32}$$

In the Y term of equation 2.28, the effective mass values for CdS are

$$m_e = 0.19m_0 \, , m_h = 0.8m_0 \, [2, \quad 40], \tag{2.33}$$

where m_0 is mass of the electron (9.10938188 × 10^{-31}kg). When the constants are substituted into Y (equation 2.28), it becomes

$$Y \cong \left(\frac{(6.582 \times 10^{-16} eV.s)^2 \times \pi^2 - nm^2}{2R^2 (nm)^2} \right) \left(\frac{0.99}{0.152 \times 9.109 \times 10^{-31} kg} \right), \tag{2.34}$$

where *R* is the radius of the nanoparticles in nanometers. In order to use equation 2.28, both sides of the equation must have the same units. In order to make unit conversion, the following relations were used:

$$1eV = 1.602 \times 10^{-19} J = 1.602 \times 10^{-19} \frac{kg \times m^2}{s^2} . \tag{2.35}$$

Thus, by using the conversion in equation 2.35, equation 2.34 can be written as

$$Y \cong \left(\frac{(4.276 \times 10^{-30})[eV.s]^2 - nm^2}{2R^2 (nm)^2} \right) \times \left(\frac{7.140 \times 10^{30}}{kg} \right) \times \left(\frac{kg \times m^2 / s^2}{J} \right) \times \left(\frac{1.602 \times 10^{-19} J}{1eV} \right) \tag{2.36}$$

By simplifying equation 2.36 the following expression can be obtained for Y:

$$Y \cong \frac{2.445[eV - nm^2]}{(R)^2 (nm)^2}. \tag{2.37}$$

To figure out the final term (Z) of equation 2.28, the dielectric constant ε for CdS must be calculated with similar conversion. For CdS material,

$$\varepsilon = 5.7\varepsilon_0 \,,\ \varepsilon_0 = 8.854 \times 10^{-12} \frac{F}{m} \text{ or } \quad \varepsilon_0 = 8.854 \times 10^{-12} \frac{C}{Vm}. \tag{2.38}$$

Substituting these constants, the following expression is obtained for the Coulomb interaction term:

$$Z \cong \frac{1.8e^2}{4 \times \pi \times 5.7 \times 8.854 \times 10^{-12} \frac{C}{V} R} \cong \frac{(1.602 \times 10^{-19})^2 eV}{6.34 \times 10^{-10} \times 1.602 \times 10^{-19} R} \cong \frac{0.455[eV - nm]}{R(nm)}. \tag{2.39}$$

By substituting equations 2.32, 2.37 and 2.39 into the equation 2.29, simplified form of Brus equation can be obtained as

$$\frac{1240[eV - nm]}{\lambda(nm)} - 2.41[eV] = \frac{2.445[eV - nm^2]}{(R)^2 (nm)^2} - \frac{0.455[eV - nm]}{(R)(nm)}. \tag{2.40}$$

The only remaining unknown in equation 2.40 is the radius of nanocrystal, *R*. This equation is valid for only CdS nanoparticles. The parameters such as effective masses and dielectric constant are variables for each material. Also, absorption spectra must be

measured. The Brus equation will be used in later chapters to determine the average radii of nanoparticles in different samples.

Chapter 3

Spectroscopic Characterization of CdS Quantum Dots

In this chapter, we investigate the influence of Poly (acrylic acid) (PAA) molecular weight and amount on nanoparticle properties such as crystal size, photoluminescence (PL) emission intensity, and quantum efficiency of CdS quantum dots. We also investigate the effect of solution pH on size and optical properties. In Section 3.1, we present the absorption measurements which are used in the determination of the size of the quantum dots. Photoluminescence setup and measurement methods are then discussed in Section 3.2. Finally, we present the results and discussion of experiments with respect to control variables (PAA amount and molecular weight, and pH value) of CdS nanoparticles.

3.1 Absorption Measurements

Celebi and Yagci prepared three sets of PAA coated CdS quantum dots with varying polymer concentration and reaction pH [11, 45]. In the characterization of the quantum dot samples, the first step was absorption measurements in the UV-Vis region. Absorption spectra of the samples were recorded with a Schimadzu UV-Vis-NIR spectrophotometer (model 3101 PC, Figure 3.1). During the measurements, the following parameters were used: (scan speed: slow, scan step: 0.5 nm, wavelength resolution: 1nm in the range 600-300 nm).

Figure 3.1: Commercial spectrophotometer used in the absorption measurements.

Quantum dot samples were placed in quartz cuvette. While absorption and transmission measurements were recorded, care was taken to obtain only the effect of CdS samples by subtracting the influence of water and the cuvette. Figure 3.2 shows the absorption spectrum of three different samples. In order to compare the samples, absorbed

excitation power should be same or close. Because of this reason, the absorption of the samples at the excitation wavelength of 355 nm was kept around 15% by controlling the amount of water.

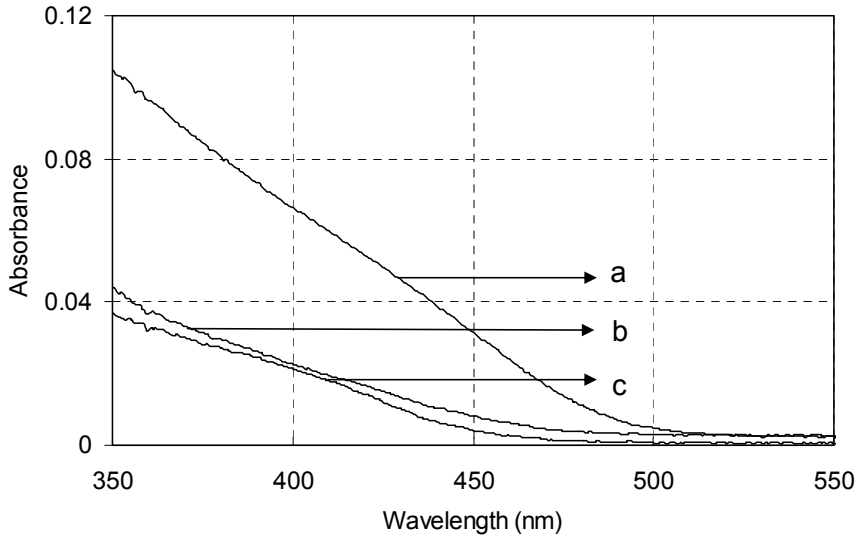

Figure 3.2: Absorption spectra of CdS nanoparticles prepared at COOH/Cd = 1.6 using (a) PAA2K at pH=5.5, (b) PAA5K at pH=7.5, (c) PAA2K at pH=7.5.

The absorption onset wavelength was used to calculate the band gap energy of the nanocrystals. In the previous chapter, Figure 2.4 shows the determination of absorption onset wavelength. By using equation 2.31, Planck's relation, the band gap values of nanoparticles were calculated. Therefore, sizes of nanoparticles were calculated by using Brus equation (Eq. 2.28). In our calculations, the bulk band gap of CdS is taken as 2.41 eV [43].

3.2 Photoluminescence Measurements

Figures 3.3 and 3.4 show the schematic and the photographs of experimental setup used in photoluminescence (PL) measurements. PL measurements were carried out at the excitation wavelength of 355 nm. A pulsed, 1064-nm Nd:YAG laser (Quantronix 116) operating at a repetition rate of 1 kHz and outputting 140 nsec pulses was used to

generate the ultraviolet (UV) pump at 355 nm. To convert the output of the Nd:YAG laser, two different crystals were used. The 1064-nm output was first frequency doubled in a 10-mm-long potassium titanly phosphate crystal (KTP) to 532 nm. The fundamental (1064 nm) and the second harmonic (532 nm) were then mixed inside a 20-mm-long lithium triborate (LBO) crystal to obtain sum frequency generation at 355 nm (45 deg. High reflective mirror at 1064 & 532 nm was used). After the LBO crystal, there exists three different wavelengths. A 355 nm band pass filter (F1) was used to cut the 1064 and 532 nm beams. LBO crystal efficiency graph (see in Figure 3.5) shows the relation between the input Nd:YAG laser power and the output UV light. Up to 36 μJ of UV light was obtained.

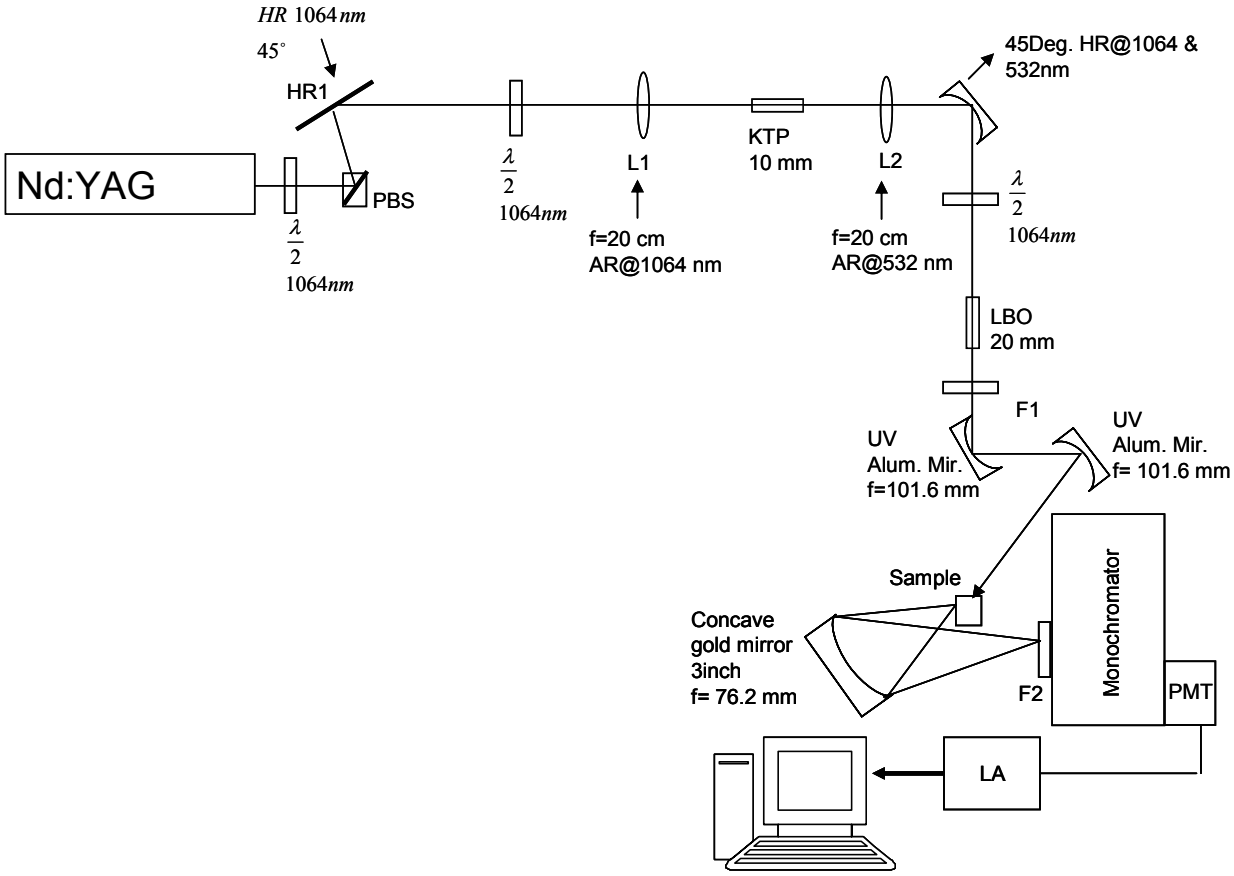

Figure 3.3: Schematic of the luminescence measurement setup.

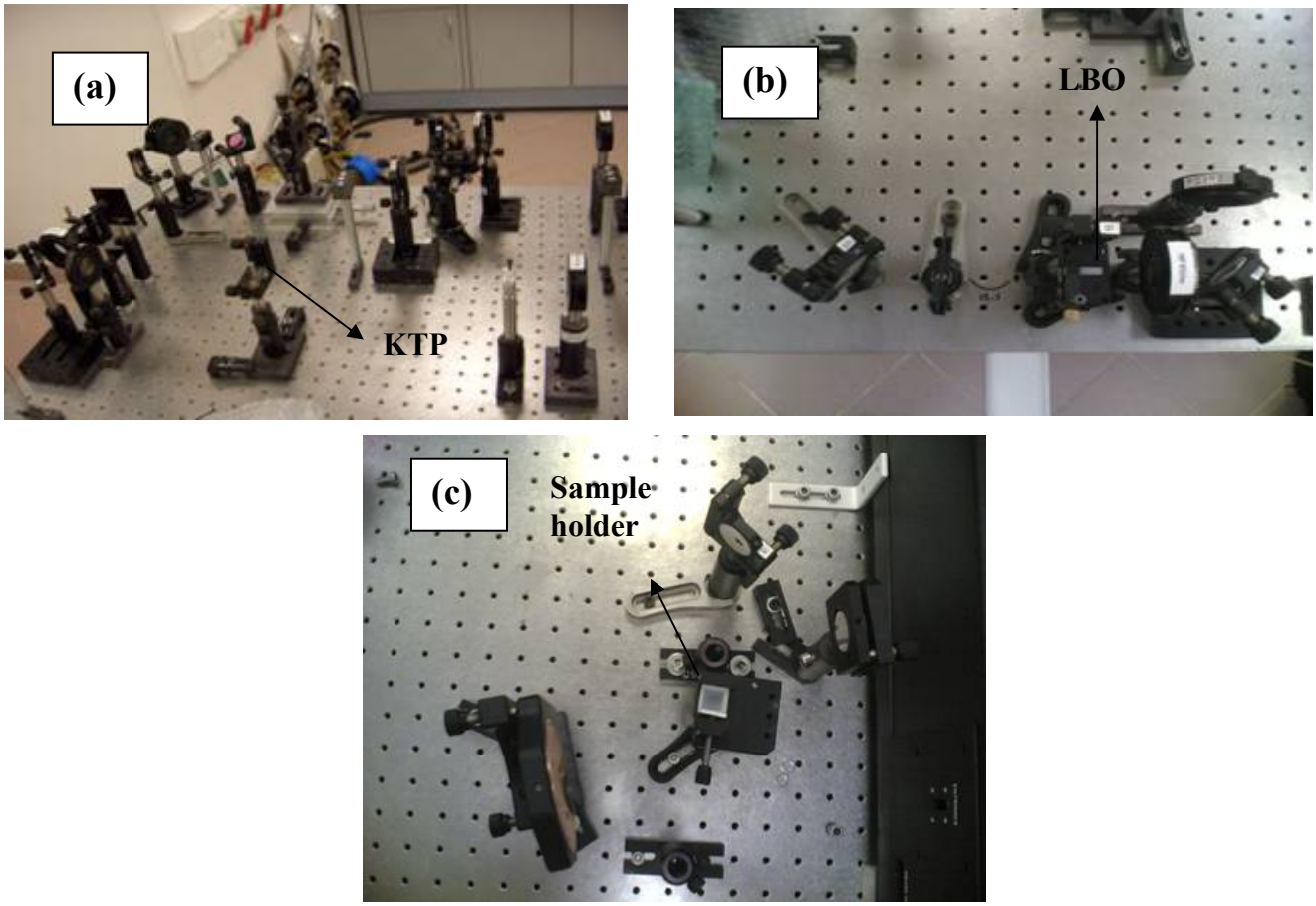

Figure 3.4: Photographs of the luminescence measurement setup: (a) generation of 532 nm light with KTP crystal, (b) generation of pump source (355 nm) with LBO crystal, (c) sample holder.

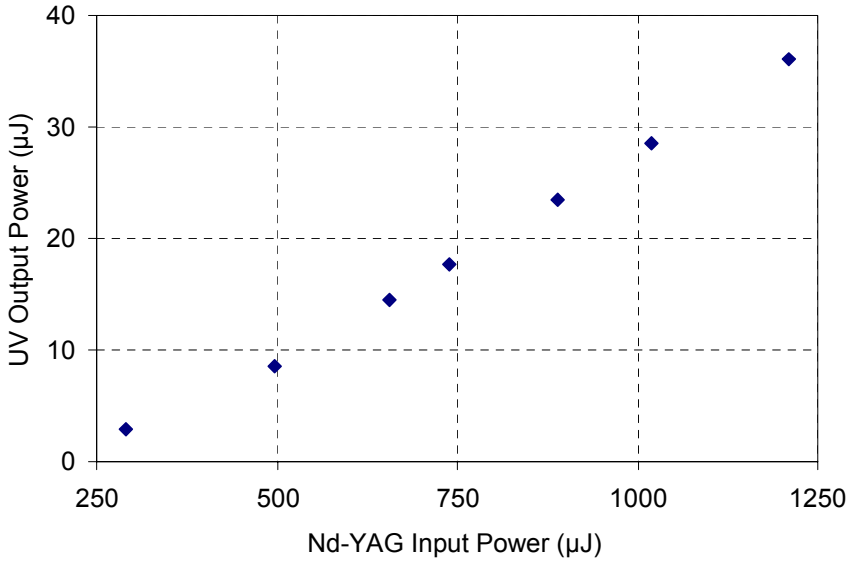

Figure 3.5: UV efficiency graph. Nd:YAG power was measured after the lens L1; UV output was measured after the filter F1. See Figure 3.3.

In the luminescence measurements, 13 μJ of UV pump energy was used. This power was measured just before the sample. Then, the pump beam was focused into the aqueous quantum dot solution with an aluminium curve mirror (f = 102 mm). The emitted fluorescence was collected with a concave gold mirror (dia: 3 inch, f: 76.2 mm) and imaged to the entrance slit of a 0.5-m, Czerny-Turner type monochromator (CVI, model DK 480). A long-pass filter (F2) was used in front of the slit to cut the light below 380 nm. The luminescence signal was detected with H957-08 Hamamatsu photomultiplier tube (PMT). PMT voltage was adjusted to 800 V. The entrance and output slit widths were set to 100 μm. The grating which works in the 330-1500 nm range was used. When the luminescence signal was obtained, it was first maximized by changing the position of the quantum dot solutions and adjusting the collecting mirror. Then, the signal was amplified with a lock-in amplifier (LIA). While measuring different samples, quantum dot solutions inside the cuvette must be changed. In order to compare the quantum yield of the samples, they must be held at the same location. A simple holder was made for this purpose as shown in Figure 3.4-c.

Emission spectra of the samples were calibrated (I_{calib}) with respect to the absorbed pulse energy at 355 nm by using the formula

$$I_{calib} = \frac{I}{Abs} \ , \tag{3.1}$$

where I is the PL intensity of the sample, Abs is the absorption at the excitation wavelength. The area under the spectrum was calculated by employing the trapezoidal method

$$Area = \Delta n\left[\frac{I_1}{2} + \left(I_2 + I_3 + ... + I_{n-1}\right) + \frac{I_n}{2}\right] , \tag{3.2}$$

where Δn is the scan step and I_n is the calibrated signal.

In order to calculate the quantum yield of the samples, we needed a reference spectrum. Rhodamine B was used as the reference material [46]. Measurement parameters of Rhodamine B must be the same with those of samples for comparison. In the first measurements of Rhodamine B, 6μmolar concentration sample with an absorption 19.78 % at 355 nm was used. In order to obtain optimum Rhodamine concentration and pump energy, series of measurements were done with Rhodamine B sample. Since pulse laser excitation was used in the quantum yield measurements, care was taken to minimize the spectral broadening of the Rhodamine B emission band. Thus, measurements at different pumping levels (for concentration = 6μmolar), and different concentrations (pumping energy = 13μJ) were performed. Figure 3.6 shows the normalized emission spectra obtained from the measurements. As the pumping energy or concentration is increased, the emission spectrum becomes broader. On the other hand, the emission band becomes narrower as the pumping energy or concentration is reduced. This effect is possibly due to of the amplified spontaneous emission (ASE). At low concentrations and pumping levels, identical spectra could be obtained. In our experiments, pump energy was kept at 13 μJ for samples. So, we had to adjust the concentration of Rhodamine B. 6μmolar Rhodamine B sample was diluted with water to an absorption level of 2.82 % at 355 nm and used in the measurements.

Then, the total integrated luminescence intensity Σ_I of each sample was used to calculate the relative luminescence quantum yield η from

$$\eta = \frac{\Sigma_I}{\Sigma_{RhB}} \ , \tag{3.3}$$

where Σ_{RhB} is the integrated luminescence intensity for Rhodamine B for the same absorbed pump power [46].

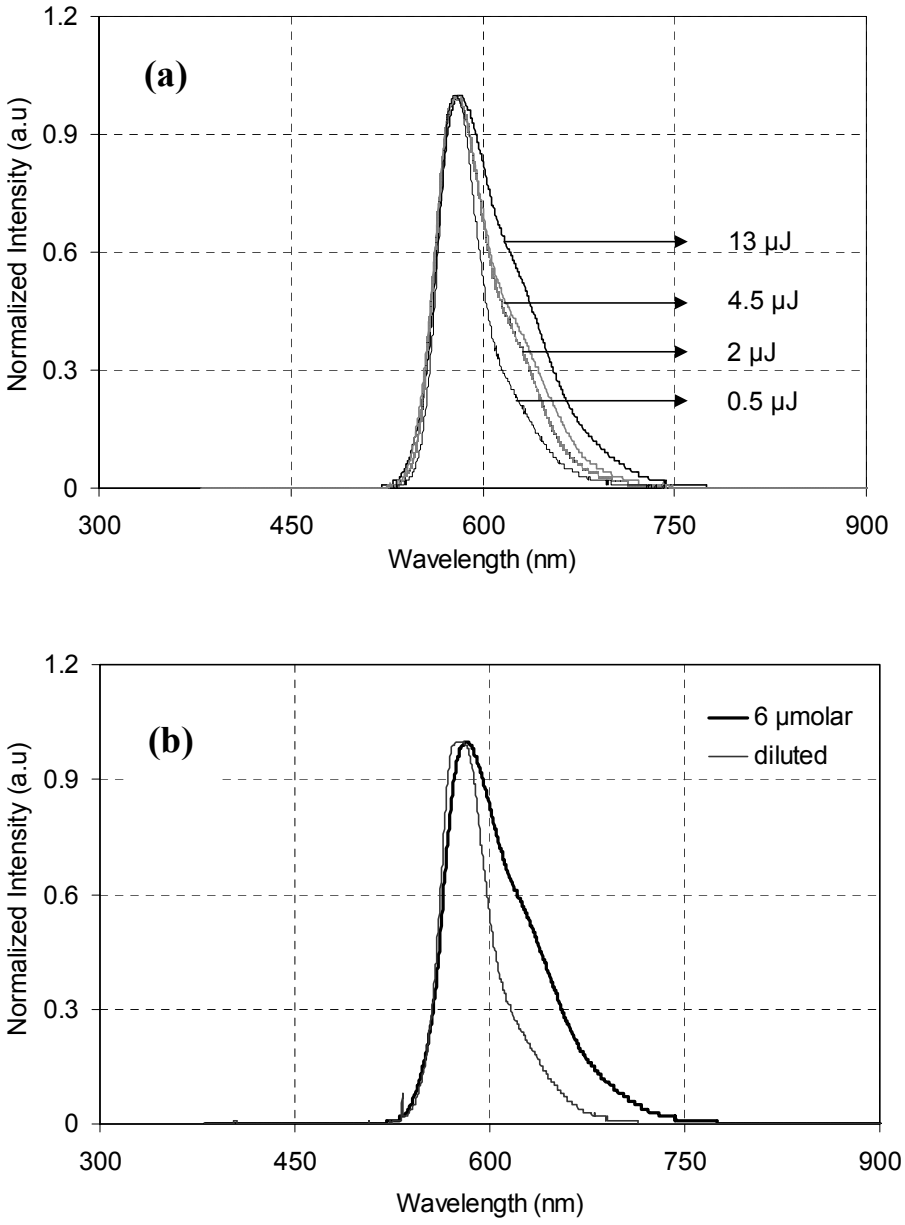

Figure 3.6: (a) Normalized PL spectra of Rhodamine B (6 µmolar) at different pump energies. (b) Normalized PL spectra of Rhodamine B at different concentration. Diluted Rhodamine B has 2.82 % absorption at 355 nm. Pump energy is 13 µJ.

3.3 Effects of Control Variables

Experiments provide results about effects of PAA amount, pH value and give quantum yields of samples with respect to these control variables. Calibrated emission spectra of samples are shown in Figures 3.7, and 3.8. In these spectra, the sharp peak at 532 nm light could not be completely filtered. Similarly, the second peak at near 404 nm is the Raman emission of water due to 355-nm excitation. These peaks were ignored in the determination of the quantum yield of the samples. The emission spectra of all samples are broad band emission, which shows a broad particle size distribution [47].

3.3.1 PAA Amount and Molecular Weight

Figures 3.7 and 3.8 show the calibrated emission spectra of samples with respect to Acid-Cd ratio (COOH/Cd), with pH=7.5 and pH=5.5 for PAA2K and with pH=7.5 for PAA5K, respectively. Increasing the amount of PAA affects the size of crystals. COOH/Cd ratio depends on the amount of PAA. This ratio increases from 1-12.5 for different PAA and pH value. For PAA2K, the particle size varies from 3.6 to 4.9 nm and for PAA5K it varies from 3.7 to 6.5 nm, at pH=7.5. Crystal size as a function of COOH/Cd ratio is also shown in Figure 3.9. When the ratios are investigated, it can be observed that crystal sizes are very close to each other around COOH/Cd ratio of 1.5-2 for both PAA molecular weights, which can be named the critical ratio for sizes. Above this ratio, increasing the amount of polymer increases the crystal size at pH=7.5. Same critical point can also be obtained from calibrated PL spectra of samples. According to Figures 3.7 and 3.8, Acid/Cd ratio around 1.5-2 is also critical for maximum PL intensity. Further increase in the coating amount causes a decrease in the PL intensity. This is quite interesting since increasing the amount of surface capping agent is generally expected to decrease the crystal size and ensure full surface coverage, decreasing non-radiative coupling. When PL intensities of PAA5K and PAA2K with pH=7.5 (Figures 3.7 (a) and 3.8) are investigated, above the critical Acid/Cd ratio, PAA5K coated CdS nanoparticles have larger crystal size (Figure 3.9) and lower PL

intensity. Negative influence of the chain length and increase in the charge density on the capping of crystal surface and arresting crystal growth could explain both outcomes.

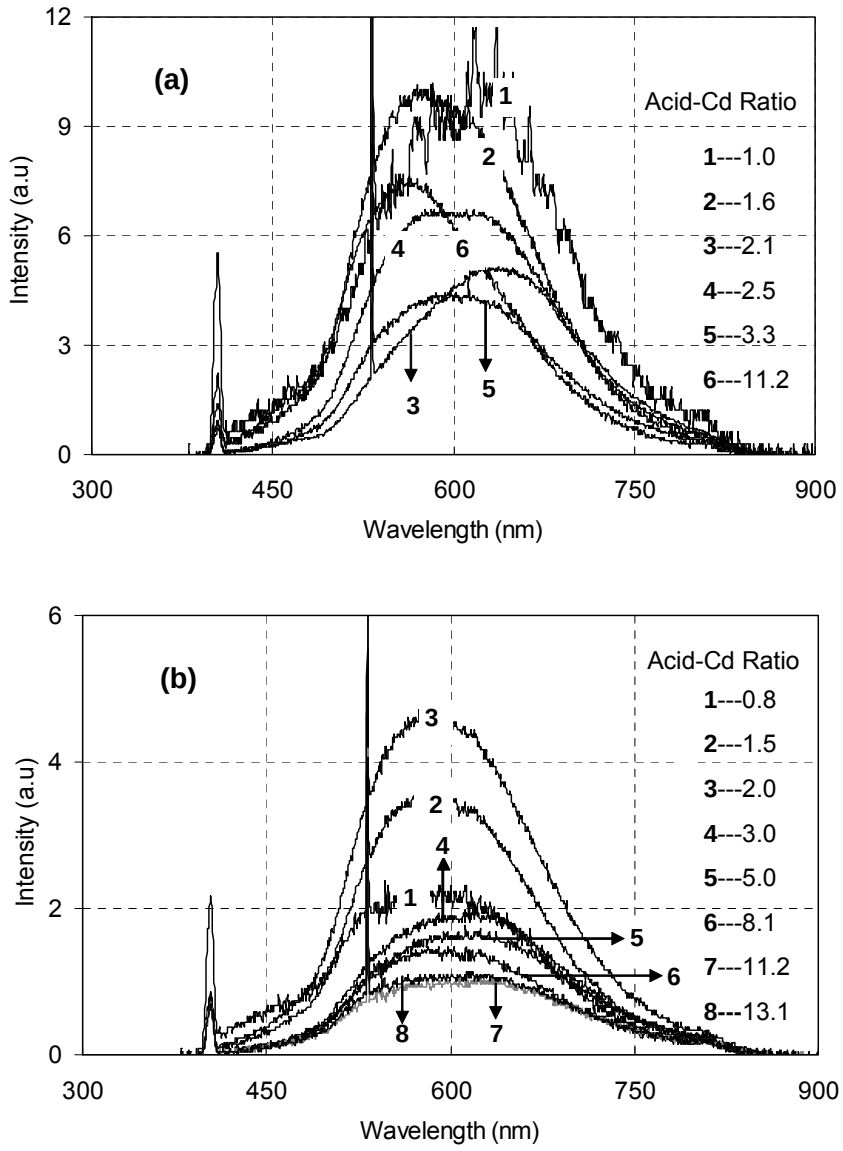

Figure 3.7: Calibrated PL spectra of PAA2K coated CdS prepared at (a) pH=7.5, (b) pH=5.5.

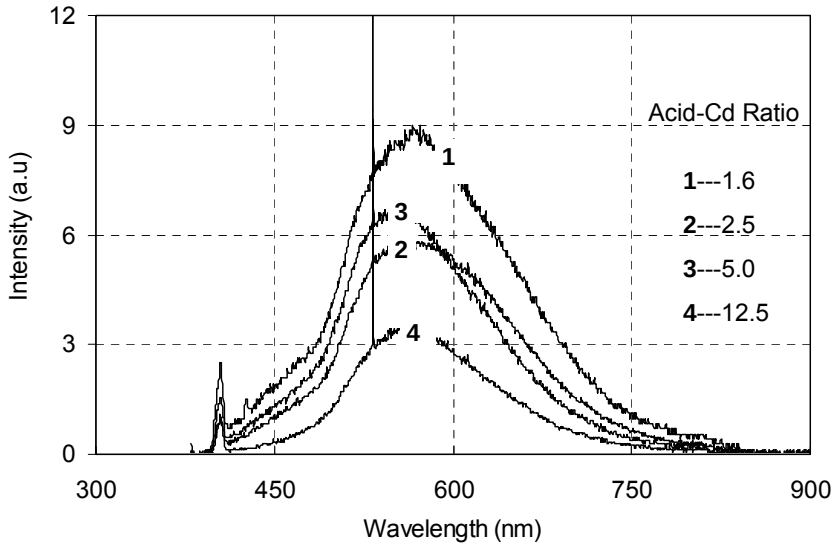

Figure 3.8: Calibrated PL spectra of PAA5K coated CdS prepared at pH=7.5.

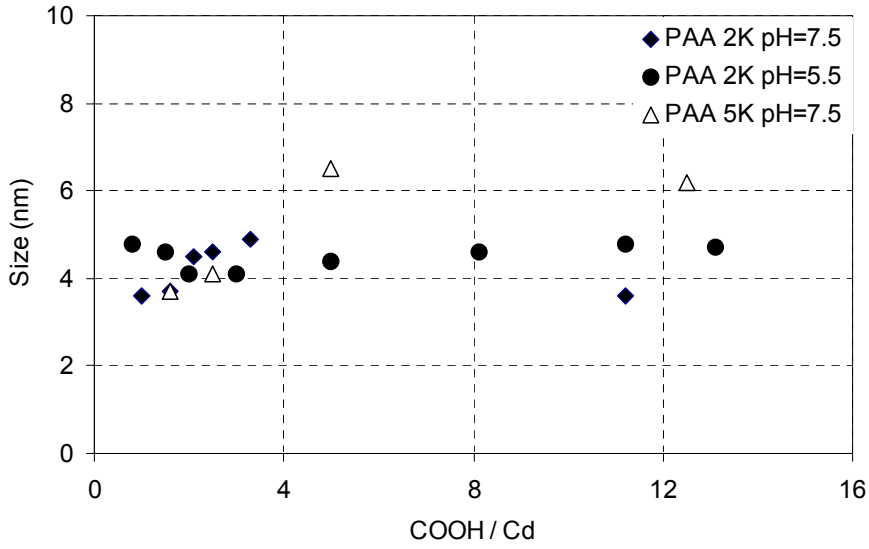

Figure 3.9: Crystal size as a function of COOH/Cd ratio for different PAA molecular weight and reaction pH.

3.3.2 pH Value

Reaction pH has a significant influence on both the crystal size and luminescence efficiencies. Although the overall variation in the crystal size as a function of COOH/Cd ratio is less dramatic at pH 5.5, as the ratio increased from 0.8 to 2, size decreased from 4.8 to 4.1nm and stayed around 4.7 nm above this ratio. This indicates the existence of a two-way interaction between the pH and the polymer amount in affecting the crystal size. At fixed COOH/Cd ratio, particles prepared at pH 5.5 absorbs at longer wavelengths (Figure 3.2) suggesting less effective surface capping as means to arrest the particle growth. When we look at Figure 3.7 (b), we observe that luminescence intensities of samples prepared with pH=5.5 dropped significantly. PL spectra showed that pH influences the optimum polymer amount required for the maximum luminescence intensity. At a pH of 5.5, PL intensity increases with increasing coating amount until the optimum COOH/Cd ratio of 2 is reached and afterwards it shows a downward trend as seen for both molecular weights at pH 7.5 and 5.5 (Figures 3.7 and 3.8).

3.3.3 Quantum Yield

Comparison of the luminescence of quantum dots and the trends observed as a function of our variables can be clearly seen in the quantum yields calculated against a reference Rhodamine B. Figure 3.10 shows the calculated relative quantum yields (η) (QY) for all samples. QY of CdS quantum dots is slightly better with PAA2K than PAA5K at pH 7.5: 8-17 % versus 5-13 %. Overall, a significant decrease in the QY is observed (around 7 %) at reaction pH 5.5. QY decreases with increasing coating amount at pH 7.5, but at pH 5.5 it has a bell-shaped trend with a maximum around COOH/Cd=2, in agreement with the PL intensity trend. Also, it is important to note that this COOH/Cd ratio is the same critical ratio observed in UV analysis and corresponds to the smallest crystal sizes for the stable colloids in each series. Smaller crystal sizes may contribute to enhanced quantum efficiency as well. This further supports the importance and

dependence of size and luminescence on polymer amount-pH interaction. Optimum COOH/Cd ratio for best QY appears to be at around the critical ratio of 1.5-2 for both molecular weights and pH.

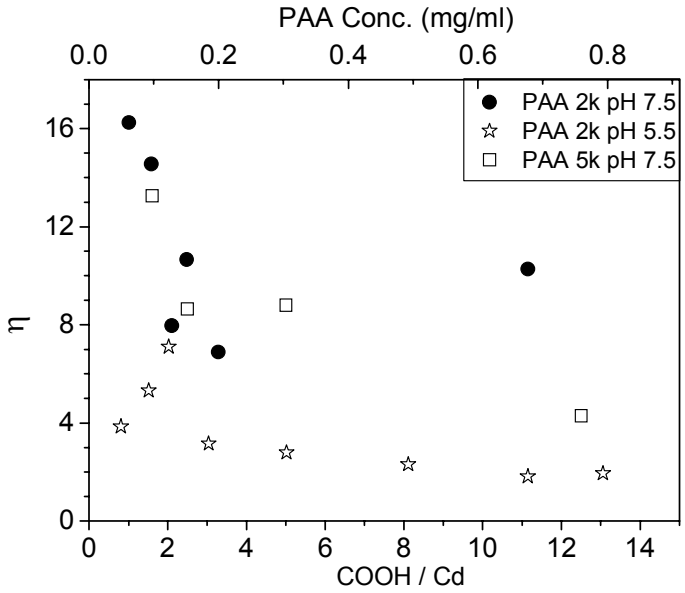

Figure 3.10: Quantum yield (η) of the samples with respect to the Rhodamine B as a function of the reaction variables.

3.4 Results and Discussions

Table 3.1 summarizes the obtained results of CdS nanoparticles. CdS quantum dots were prepared successfully in a simple aqueous solutions with PAA coating of 2100 and 5000 g/mol molecular weight. Calibrated emission spectra of CdS quantum dots show that these particles are luminescent mostly in the light yellow-orange part of the electromagnetic spectrum. They have an absorption in the range of 460-508 nm. The changes in the amount and molecular weight of PAA (COOH/Cd in the range of 0.8-12.5) cause small differences in sizes between 3.6 to 6.5 nm. However, obtained sizes (Table 3.1) and PL spectra show that there is broad particle size distribution [47]. PAA provides surface adsorbing groups that are dependent on each other. The chain

conformation is affected by the repulsion of neighboring groups which enables the growing and prevents adsorption on the crystal surface. Thus, it causes limited size tuning. Carboxylates of PAA adsorb on Cd^{2+} rich surface much more effectively, and therefore, Cd/S ratio above 1 is desirable for better surface capping, enabling better size control and better luminescence. Thus Cd/S ratio is fixed to 1.1.

Sample ID*	COOH / Cd	Cd / S	Absorption onset (λ_{nm})	Size[a] (nm)	Band gap[b] (eV)	FWHM[c] (nm)
PAA 2K-1a	1.0	1.1	460	3.6	2.70	181.5
PAA 2K-2a	1.6	1.1	464	3.7	2.68	161.0
PAA 2K-3a	2.1	1.1	486	4.5	2.55	176.5
PAA 2K-4a	2.5	1.1	488	4.6	2.54	179.5
PAA 2K-5a	3.3	1.1	492	4.9	2.52	177.0
PAA 2K-6a	11.2	1.1	459	3.6	2.71	153.0
PAA 2K-1b	0.8	1.1	490	4.8	2.53	189.5
PAA 2K-2b	1.5	1.1	487	4.6	2.55	163.5
PAA 2K-3b	2.0	1.1	477	4.1	2.60	165.5
PAA 2K-4b	3.0	1.1	477	4.1	2.60	182.5
PAA 2K-5b	5.0	1.1	484	4.4	2.57	193.5
PAA 2K-6b	8.1	1.1	488	4.6	2.54	173.0
PAA 2K-7b	11.2	1.1	490	4.8	2.53	196.5
PAA 2K-8b	13.1	1.1	489	4.7	2.54	201.5
PAA 5K-1a	1.6	1.1	463	3.7	2.68	161.0
PAA 5K-2a	2.5	1.1	476	4.1	2.61	160.5
PAA 5K-3a	5.0	1.1	508	6.5	2.44	143.0
PAA 5K-4a	12.5	1.1	506	6.2	2.45	133.5
PAA 5K-5a	1.6	2.5	470	3.9	2.64	164.5
PAA 5K-6a	1.6	0.6	490	4.8	2.53	152.5

Table 3.1: Average size and band gap of CdS nanoparticles calculated from UV-Vis spectra, **a**: synthesized at pH=7.5, **b**: at pH 5.5, [a] calculated by Brus effective mass approximation, [b] corresponding band gap energy, [c] full width half maximum calculated from PL spectra.

QYs of the PAA coated CdS quantum dots are in the range of 5-17%. A very important outcome of this study is the identification of an optimum COOH/Cd ratio around 1.5-2 for the highest PL intensity and QY for both molecular weights and pH (5.5 and 7.5) within the limits of colloidal stability. pH effect is investigated, and we realized that it is also critical parameter for the QY and particle size. Particles prepared at higher pH values have higher QY due to better surface passivization.

This work is the first detailed study of PAA coated CdS nanoparticles [11]. In spite of having colloidal stability, PAA coated CdS nanoparticles do not have very high QY. It is possible to improve the luminescence intensity and QY of these particles further by coating CdS crystals with ZnS or CdSe/ZnS as described in the literature [48-50]. The knowledge gained from this study can be applied to other polymers and quantum dots.

Chapter 4

Saturation Analysis of Fe^{2+}:ZnSe

Over the last years, Fe^{2+}:ZnSe crystal has been demonstrated as a mid-infrared laser medium [13, 24-28]. In addition, this material can also be used as a saturable absorber for lasers working around 3μm [29, 30]. In this chapter, we investigate the saturation analysis of Fe^{2+}:ZnSe crystal. In order to determine the saturation parameters such as absorption cross section ($\sigma_a(\lambda)$), normalized excited-state absorption cross section (f_p) values at the wavelengths of 2645 and 2730 nm, a best-fit algorithm was used. Determination of the absorption cross section provides a convenient method to measure the concentration of sample. In section 4.1, the theoretical model is presented for analysis of experimental data, especially for pulsed case. Experimental set-up, application of best-fit algorithm and its results are discussed in section 4.2. Then the obtained $\sigma_a(\lambda)$ and f_p values are compared to reported values in the literature.

4.1 Theoretical Model

If Fe ion concentration (N_{Fe}) of Fe^{2+}:ZnSe crystal is known exactly, absorption cross section at a given wavelength can be obtained by the formula:

$$\sigma_a(\lambda) = \frac{\alpha_{p0}(\lambda)}{N_{Fe}}, \tag{4.1}$$

where $\alpha_{p0}(\lambda)$ is the measured absorption coefficient of the sample. When iron ion concentrations of samples are not known definitely, absorption cross section value can be determined by saturation measurements. In these measurements, operating laser wavelength must coincide with the absorption band of the sample. These measurements can be performed with two different methods. In the first method, transmitted power

(cw case) or energy (pulsed case) of the sample is measured by changing the focus position at a fixed incident pump power (z-scan method). In the second method, the transmission of the sample with respect to laser power or energy change is measured. In this theoretical model, rate equation analysis will be discussed based on 4-level energy systems [51]. Figure 4.1 shows the transitions between the energy levels of a 4 level system.

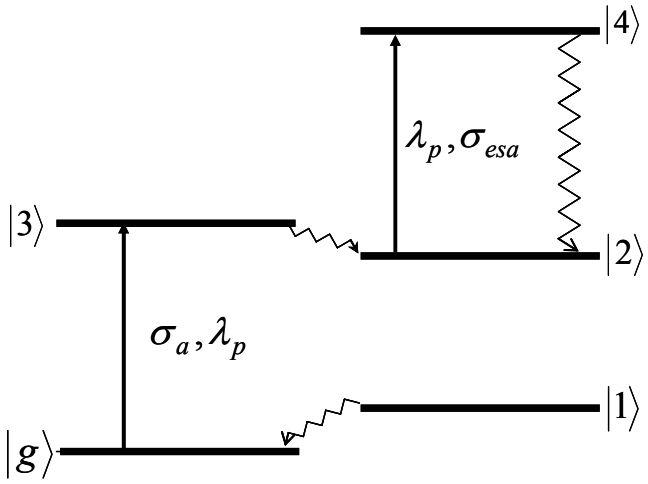

Figure 4.1: Energy level diagram for Fe:ZnSe crystal (4-level system), with the possibility of excited state absorption. σ_{esa} is excited state absorption cross section. σ_a is the absorption cross section, λ_p is the pump wavelength.

When the pump photons at the wavelength of λ_p coincide with absorption band of the material, transitions occur between the energy levels. By the absorbed photons, ions in the ground state ($|g\rangle$) make transitions to the upper energy level $|3\rangle$. Then, they decay to the second energy level ($|2\rangle$) as a result of a non-radiative process. For Fe:ZnSe crystal, laser emission occurs around 4 μm due to stimulated emission from the second energy level. In our analysis, we will ignore the stimulated emission from second energy level to first energy level ($|1\rangle$), and assume that only spontaneous emission occurs. Then ions in the first energy level decay very rapidly to the ground energy level. In addition to these transitions, the ions in the second level can also absorb photons at

the wavelength of λ_p, and make transitions to the upper level ($|4\rangle$). This process is called excited-state absorption and σ_{esa} is the excited-state absorption cross section. Excited ions in level 4 also decay rapidly to second level. The interactions above obey the following rate equations:

$$\frac{\partial N_2}{\partial t} = -\frac{\partial N_g}{\partial t} = \frac{\sigma_a I_p \lambda_p}{hc} N_g - \frac{N_2}{\tau_f}, \tag{4.2}$$

where h is Planck's constant, c is the speed of light, I_p is the intensity of the pump radiation at λ_p, σ_a is the ground-state absorption cross section at λ_p, τ_f is the fluorescence lifetime, N_g is the population density of ions in the ground-state and N_2 is the population density of ions in the second state. Ion populations N_4, N_3 and N_1 are negligible when they are compared with N_g and N_2. So we did not take into account these ion populations in equations 4.2.

Next, consider a thin slab of the saturable absorber with a cross sectional area *A* and thickness *dz*, as shown in Figure 4.2.

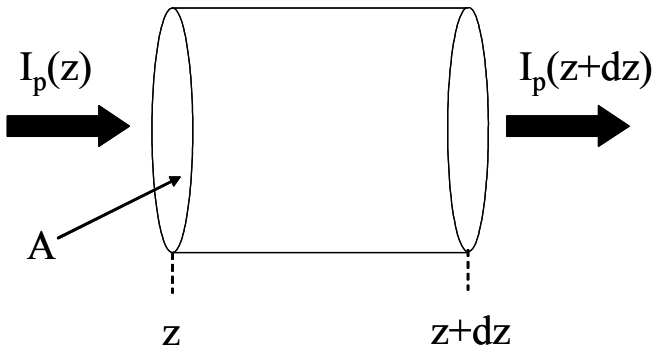

Figure 4.2: Thin slab of the saturable absorber with cross sectional area *A* and thickness *dz*.

Conservation of energy gives

$$Adz\frac{\partial u_p}{\partial t} = \left[I_p(z) - I_p(z+dz)\right]A - \left(N_g \sigma_a I_p + N_2 \sigma_{esa} I_p\right)Adz, \tag{4.3}$$

where u_p is the electromagnetic energy density at the wavelength λ_p, and second term of the right hand-side of the equation corresponds to the pump energy lost. The expression can be simplified by using the relation $u_p v_g = I_p$ (v_g = group velocity):

$$\frac{\partial I_p}{\partial z} + \frac{1}{v_g}\frac{\partial I_p}{\partial t} = -\sigma_a I_p (N_g + f_p N_2). \tag{4.4}$$

Here, f_p is the normalized excited state absorption cross section at λ_p and denoted as

$$f_p = \frac{\sigma_{esa}(\lambda)}{\sigma_a(\lambda)}. \tag{4.5}$$

Furthermore, the sum of ion population density at ground energy level (N_g) and second energy level (N_2) give us the total Fe ion population density of the material:

$$N_{Fe} = N_g + N_2. \tag{4.6}$$

By using equations 4.2 and 4.6, equation 4.4 can be written as

$$\frac{\partial I_p}{\partial z} + \frac{1}{v_g}\frac{\partial I_p}{\partial t} = (1 - f_p)\frac{\partial N_g}{\partial t} h v_p - I_p f_p \alpha_{p0}, \tag{4.7}$$

where α_{p0} is the small signal differential absorption coefficient at λ_p and discussed in equation 4.1. In our analysis we assume that pulsewidth of the laser is much shorter than the lifetime of material. The pulsed intensity $I_p(t)$ and the integrated energy density $\overline{E}_p$ are related by the expression

$$\int_{-\infty}^{\tau} dt I_p(t) = \overline{E}_p. \tag{4.8}$$

where τ is larger than the pulsewidth. So that pump intensity vanishes at τ $(I_p(\tau) = 0)$. If we substitute equation 4.8 into the equation 4.7 and integrate with respect to time from -∞ to τ, the following expression is obtained:

$$\frac{\partial \overline{E}_p}{\partial z} = (1 - f_p) h v_p \left(N_g(\tau) - N_{Fe}\right) - \overline{E}_p \sigma_{esa} N_{Fe}. \tag{4.9}$$

In equation 4.9, we assume that initial as $N_g(-\infty) = N_{Fe}$. Integrating equation 4.2 over the same intervals by using the assumption that τ is much shorter than the fluorescence lifetime τ_f, we obtain the relation between the ion population density of the ground level and total ion population density as

$$N_g = N_{Fe} \exp\left(-\frac{\overline{E}_p}{E_{sa}}\right), \tag{4.10}$$

where E_{sa} ($E_{sa} = h\nu_p / \sigma_a$) is the absorption saturation fluence. Substituting this equation into the equation 4.9 gives

$$\frac{\partial \overline{E}_p}{\partial z} = -(1-f_p)\alpha_{p0}E_{sa}\left[1-\exp\left(-\frac{\overline{E}_p}{E_{sa}}\right)\right] - \overline{E}_p\alpha_{p0}f_p. \tag{4.11}$$

The relation between the pulse energy density and the total energy per pulse is given by the expression

$$\overline{E}_p = E_p\Phi_p, \tag{4.12}$$

where Φ_p is the normalized distribution function. For Gaussian beams, it is given by

$$\Phi_p = \frac{2}{\pi w_p^2}\exp\left(-\frac{2r^2}{w_p^2}\right), \tag{4.13}$$

where w_p is the position-dependent spot size function. If we substitute equation 4.13 and 4.12 into the equation 4.11 and integrate over the beam cross section, we obtain pump energy change per unit area in the saturable absorber in terms of the total pump energy per pulse as

$$\frac{\partial E_p}{\partial z} = -(1-f_p)\alpha_{p0}E_{sa}\int_0^\infty dr 2\pi r\left[1-\exp\left(-\frac{E_p\Phi_p}{E_{sa}}\right)\right] - E_p\alpha_{p0}f_p. \tag{4.14}$$

Transmission of the material depends both on the pump pulse energy and focused position of pump pulse inside the material. Equation 4.14 will be used in the analysis of experimental data taken with Fe^{2+}:ZnSe sample.

4.2 Experimental Results

Figure 4.3 and 4.4 show schematic and photograph of the experimental setup used in the saturation measurements. In the experiments, tunable Cr^{2+}:ZnSe laser was used as the pump source [52]. The laser light was focused on the Fe^{2+}:ZnSe crystal by using a lens with 3.5 cm focal length. The transmitted power was measured with a power meter (Coherent, Model PowerMax 5200). Corresponding transmitted energy was determined by dividing the average power by the pulse repetition rate which is 1 kHz in our case.

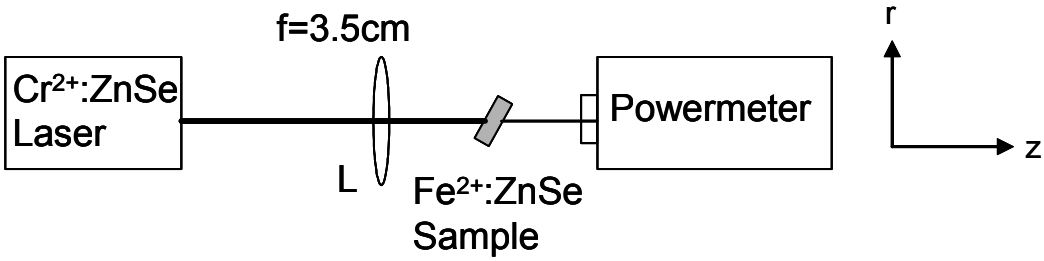

Figure 4.3: Schematic of experiment setup.

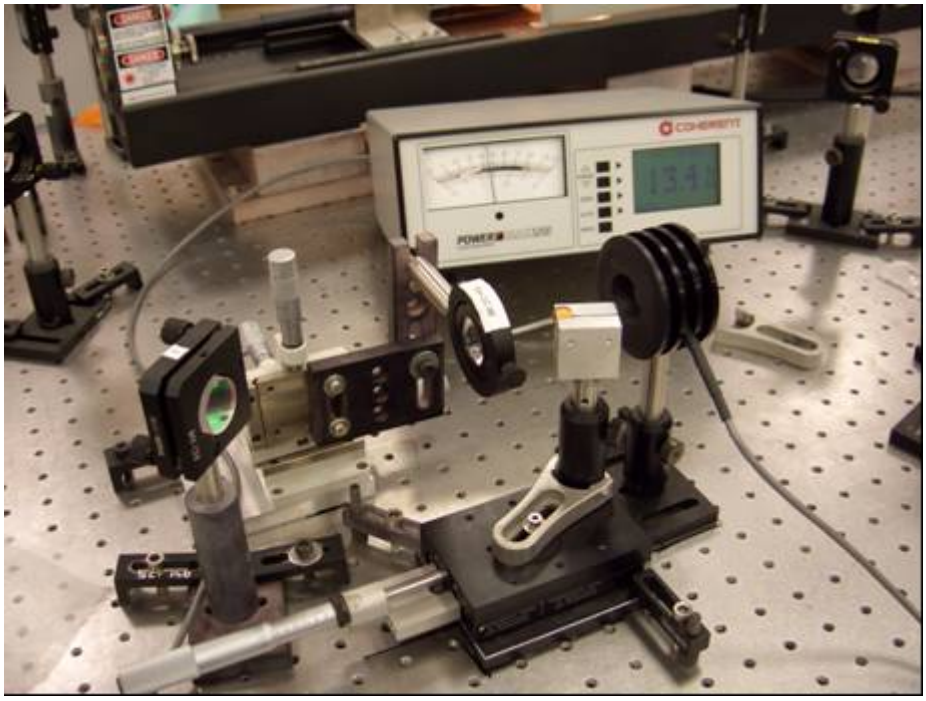

Figure 4.4: Photograph of the experimental setup for saturation measurements.

In saturation measurements, pump spot-size function is another parameter that must be measured. Spot size ($w_p(z)$) measurements were performed by using the knife-edge technique. In this technique, a vertical razor blade was used. It was scanned across the beam cross section to determine the transverse locations x_1 and x_2 which gave 84% and 16% power transmission, respectively. The difference $|x_2 - x_1|$ between the locations gives the spot size at that location. In order to determine the beam parameters, the spot size function is written as

$$w_p(z) = w_{p0}\left[1 + \left(\frac{z - z_{fp}}{z_{Rp}}\right)^2\right]^{1/2}, \tag{4.15}$$

where w_{p0} is the pump beam waist, z_{fp} is the beam-waist location, and z_{Rp} is the Rayleigh range. The beam waist was determined to be 14 μm with a value of M^2=1 by using best-fit algorithm. Figure 4.5 shows measured and fit spot-size function with respect to position.

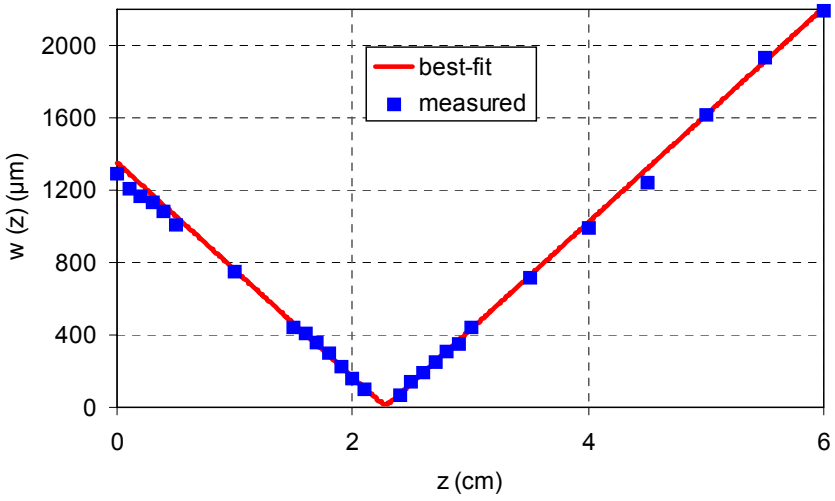

Figure 4.5: Measured and fit variations of the spot-size function as a function of position.

The sample was placed near the focal point of the lens and located at Brewster incidence to minimize the reflection losses from the surfaces. The cylindrical

polycrystalline ZnSe samples with 10 mm diameter were supplied by Crystran Ltd., and Fe was added by thermal diffusion doping technique [23]. Our sample has Fe ion concentration of approximately 6.8 x 10^{18} ion/cm^3 and a length of 1.98 mm. After determination of the beam-waist, we adjusted the output wavelength of our pump source 2645 and 2730 nm for two measurements, respectively. We used two methods in order to measure the transmission of the sample. In the z-scan method (first method), the transmission of the pump source is measured with respect to position of the Fe^{2+}:ZnSe crystal. By this method the spot size was varied by translating the samples along the optical axis. In the second method, we measure the variation of transmission as a function of incident power. We used a best-fit algorithm for both methods in order to analyze the experimental data. In the best-fit analysis, equation 4.14 was used to model the saturation of Fe^{2+}:ZnSe. For initial α_{p0}, σ_a and f_p values, equation 4.14 is solved and the standard deviation between the experimental and theoretical transmission calculated. Then, α_{p0}, σ_a and f_p values are changed until the standard deviation is minimized. By this way, for two different pump wavelengths, best-fit values of α_{p0}, σ_a and f_p were determined with both methods. Best-fit parameters are summarized in Tables 4.1 and 4.2. Figures 4.6 and 4.7 show experimental and best-fit transmission results for both methods and wavelengths.

pump wavelength (λ)(nm)	**α_{p0}(m^{-1}) Spectrometer value**	**α_{p0}(m^{-1}) Best fit value**	**f_p value $\sigma_a(\lambda)$ / $\sigma_{esa}(\lambda)$**	**$\sigma_a(\lambda)$ ($10^{-19}cm^2$)**
2645	614	764	0.09	1.35
2730	866	1015	0.04	1.97

Table 4.1: The best-fit saturation parameters of the Fe^{2+}:ZnSe sample at two different wavelength for the z-scan method (first method).

pump wavelength (λ)(nm)	**α_{p0}(m^{-1}) Spectrometer value**	**α_{p0}(m^{-1}) Best fit value**	**f_p value $\sigma_a(\lambda)$ / $\sigma_{esa}(\lambda)$**	**$\sigma_a(\lambda)$ ($10^{-19}cm^2$)**
2645	614	852	0.36	2.1
2730	866	1141	0.29	2.96

Table 4.2: The best-fit saturation parameters of the Fe^{2+}:ZnSe sample at two different wavelength for the power saturation method.

Best-fit $\alpha_{p0}(\lambda)$ values differ from spectrometer values for both methods. This result is due to the fact that pulsed pump source was used. In the pulsed case, small-signal transmission data are not sufficient to estimate $\alpha_{p0}(\lambda)$, since saturation starts even at low incident power.

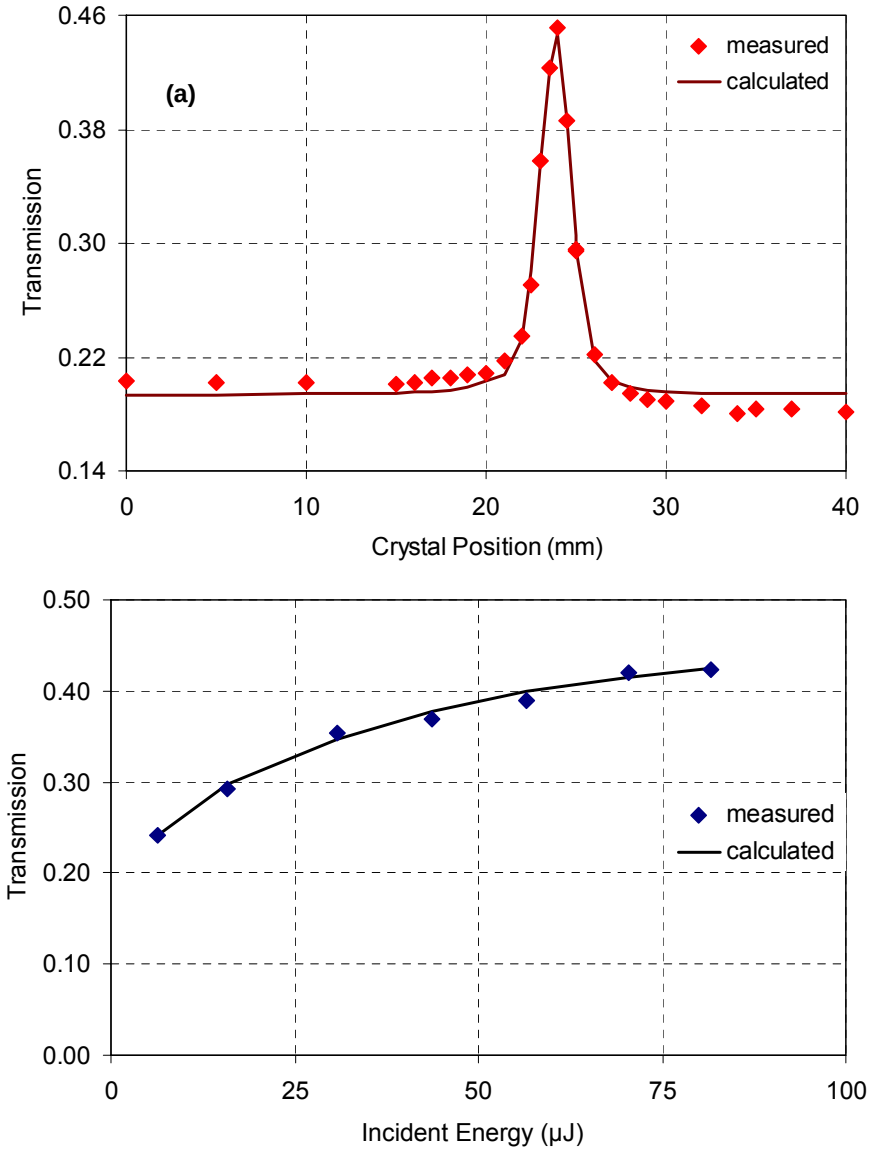

Figure 4.6: Measured and calculated transmission at 2645 nm as a function of the (a) crystal position (incident pump energy = 84 μJ) and (b) incident energy.

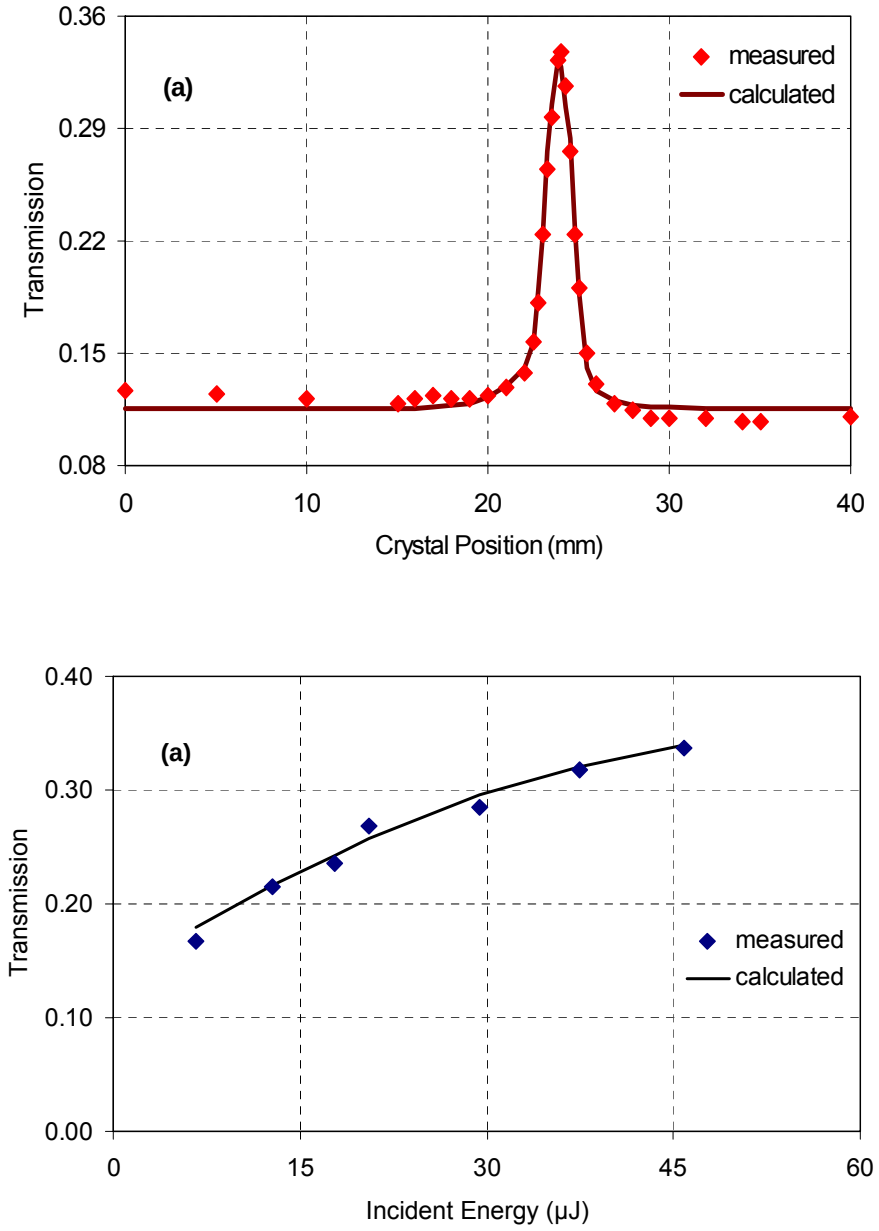

Figure 4.7: Measured and calculated transmission at 2730 nm as a function of the (a) crystal position (incident pump energy = 53 μJ) and (b) incident energy.

However, if we investigate the ratios of spectrometer and best fit $\alpha_{p0}(\lambda)$, it can easily be observed that they are close to each other. The spectrometer $\alpha_{p0}(\lambda)$ ratio, z-scan

method and second method $\alpha_{p0}(\lambda)$ ratios are 1.41, 1.32 and 1.34, respectively. According to the equation 4.1, spectrometer $\alpha_{p0}(\lambda)$ ratio and $\sigma_a(\lambda)$ must be consistent. Spectrometer absorption ratio for different wavelength is $\alpha_{p0}(2730)/\alpha_{p0}(2645) \cong 1.41$ as discussed above. The ratio of the best-fit $\sigma_a(\lambda)$ values at two wavelengths ($\sigma_a(2730)/\sigma_a(2645)$) for the first method (z-scan method) is 1.46. It is 1.41 for the second method. The percentage errors of the best-fit ratio with respect to spectral absorption coefficient are ≈ 3.5%, and ≈ 0% for first and second method, respectively. Obtained $\sigma_a(\lambda)$ values (Tables 4.1 and 4.2) are different for both methods. But, the ratios are consistent for each method. In addition, $\sigma_a(\lambda)$ values are less than the literature values ($\sigma_a(2790nm) \cong 5\times10^{-19} cm^2$ [30], $\sigma_a(2698nm) \cong 6.5\times10^{-19} cm^2$ [24]). Variations in host material may cause these differences.

On the other hand, there is a wider range of f_p values for these methods. The obtained f_p values by the first method indicate that the excited-state absorption is negligible as found in reference [30]. The results of the power transmission method are unexpected. Therefore, for both methods the average value of absorption cross section and (σ_a) and normalized excited-state absorption cross section (f_p) are determined to be 1.73×10^{-19} cm^2 and 0.23 at 2645 nm. At the wavelength of 2730 nm, these values are 2.47×10^{-19} cm^2 and 0.17. The ratio of average best-fit values of $\sigma_a(\lambda)$ at two wavelength ($\sigma_a(2730)/\sigma_a(2645)$) is ≈ 1.43 which is also consistent with the spectrometer absorption ratio ($\alpha_{p0}(2730)/\alpha_{p0}(2645) \cong 1.41$).

Chapter 5

Trials of Lifetime Measurement and Lasing in Fe^{2+}: ZnSe

Iron ion-doped chalcogenide crystals such as Fe^{2+}:ZnSe are potentially important solid state laser gain media due to their strong, broad absorption and emission in the mid-infrared region. In this chapter, we first review the previous studies performed with Fe^{2+}:ZnSe crystals, which proved that laser emission is possible at low and room temperature. We first attempted to characterize Fe^{2+}:ZnSe samples at cryogenic temperatures. In order to perform the low temperature measurements, a cryogenic system was developed. The design is discussed in Section 5.2. Finally, we discuss our attempts for lifetime measurements at both low and room temperature, as well as laser trials at room temperature with two Fe^{2+}:ZnSe crystals. So far, we have not manage to observe fluorescence and lasing near 4 μm.

5.1 Literature Review

In 1996, Deloach et al. reported that chalcogenide crystals such as ZnS, ZnSe, and ZnTe, which are doped with transition metal (TM) ions like Cr^{2+}, Ni^{2+}, Co^{2+} ,and Fe^{2+} have potential applications as room-temperature, mid-infrared tunable laser media in the 2-5 μm range [19]. Among these media, Cr has the highest gain at room temperature and wide-band emission in the 2-3 μm region. The first laser demonstration of Cr^{2+}:ZnSe crystal was performed by Page et al [20]. The success in the Cr:ZnSe laser has motivated further research into other TM ion doped chalcogenide crystals. The lack of a widely tunable lasers operating in the 3-5 μm range is the main reason for working on Fe ion doped II-VI crystals. The Cr^{2+} ion has four electrons in its d shell (d^4) while Fe^{2+} has six electrons (d^6). Because of this, energy levels are inverted. Figure 5.1 shows the simplified energy level diagram of the Fe^{2+} ($3d^6$) ion. The ground level of the Fe^{2+} ion splits into the ^5E and $^5T_2$ energy levels inside ZnSe host by the crystal field. The energy level splitting of Fe^{2+} is smaller than that of Cr^{2+} that is why Fe^{2+}:ZnSe laser is expected to operate at longer wavelengths [15, 24].

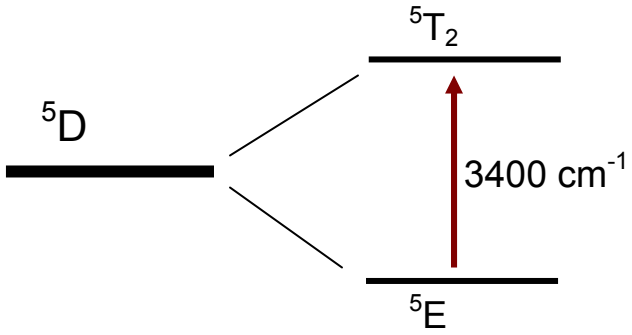

Figure 5.1: Energy level diagram of Fe^{2+} in ZnSe. ^5D energy level of the Fe^{2+} ion splits into ^5E and $^5T_2$ energy levels under the influence of the crystal field. Splitting is estimated to be around 3400 cm^{-1}[13].

The first Fe^{2+}:ZnSe laser was demonstrated by the Lawrence Livermore researchers, Adams et al., in 1999 [24]. Single crystal samples prepared with Bridgman-growth method with different Fe ion concentrations between 3.41 to 6.53 x 10^{19} ions/cm^3 were used in the experiments. The pump was an Er:YAG laser operating at 2.698 μm. Absorption cross sections for pump source were 2.9 x 10^{-19} and 6.5 x 10^{-19} cm^2 at 14 and 300 K, respectively. Lasing of the Fe^{2+}:ZnSe crystal was obtained in the temperature range from 15 to 180 K. In the experimental setup, a cryogenic chamber was used to cool the Fe^{2+}:ZnSe crystal. The sample was placed between two identical 10 cm concave mirrors. The output wavelength of the Fe^{2+}:ZnSe laser was observed to tune with temperature. It operated at 3.98 μm at 15 K and 4.54 μm at 180 K. The highest output pulses had an energy of to be 12 μJ with a duration of 48 μs. The absorbed pump energy was111.2 μJ.

In later studies, Akimov et al. obtained laser operation in a different spectral range of laser emission [25]. In particular, lasing of Fe^{2+}:ZnSe was observed to tune from 3.77 to 4.40 μm with a pump radiation of 2.9364-μm from an Er:YAG laser. In this work, Fe^{2+}:ZnSe single crystals grown from the vapor phase by the free growth technique were used. All experiments were performed at liquid nitrogen temperature. Instead of liquid nitrogen, thermoelectric cooler was used for the first time to cool the laser crystal by Voronov et al [26]. Flash lamp pumped free-running 2.9364-μm Er:YAG laser was the pump source. Generation of Fe^{2+}:ZnSe laser was observed in the 85-255 K temperature range. The slope efficiency of the laser decreased with the temperature from 43% (85 K) down to 9% (255 K). The emission spectrum of Fe^{2+}:ZnSe laser was shifted from 4.0 to 4.17 μm in this temperature range.

The first room-temperature Fe^{2+}:ZnSe laser operated in the 3.9-4.8 μm spectral range [27]. Polycyrsytalline samples were grown by chemical vapor deposition and doped with Fe ion by thermal diffusion method. The calculated iron ion concentration in the crystals was about 6-8 x 10^{18} ions/cm^3. Absorption cross section of the samples was estimated in reference [24]. The main pump source operated at 2.92 μm which is obtained by the 2^{nd} Stokes radiation of Q-switched Nd:YAG laser with a repetition rate

of 10 Hz, and pulse duration of 7 ns. The pulse duration of the pump system was shorter than the lifetime of the excited state of Fe^{2+}:ZnSe, which is one of the advantages of room temperature studies. The crystal temperature remained 300 K during the experiments. The laser cavity was formed by a gold mirror and the Fresnel reflection from the output face of the crystal. Further room-temperature study of the Fe^{2+}:ZnSe laser was performed by Fedorov et al [28]. Spectroscopic properties of Fe^{2+}:ZnSe and co-doped Fe^{2+}:Cr^{2+}:ZnSe crystals were studied at room and low temperature [25-27]. In addition, microchip lasing of Fe^{2+}:ZnSe crystal at 4.4 μm was demonstrated at room temperature. The Fe^{2+}:ZnSe crystals were excited at 2.92 μm with a 5ns pulse [28]. The output spectrum of the room temperature Fe^{2+}:ZnSe laser was tuned in the 3.95-5.05 μm range. So, the overall tuning range demonstrated in these studies was from 3.77 to 5.05 μm.

5.2 Cryogenic System Design and Construction

Mid-infrared transitions in the Fe^{2+}:ZnSe crystal undergo multi-phonon quenching at room temperature[28]. For transition metal ions, large part of the nonradiative decay is multi-phonon relaxation [12]. The rate of multi-phonon relaxation is temperature-dependent [53]. When the temperature increases, multi-phonon relaxation rate increases. Therefore, nonradiative decay processes become dominant in the crystal. Because of this reason, in order to perform lifetime measurements and laser trials, first we decided to cool our samples. For this purpose, we designed a simple cryogenic system. This system consists of Fe^{2+}:ZnSe crystal holder, vacuum chamber, vacuum valve, and cold finger parts.

Figure 5.2 shows the drawing and photograph of crystal holder part. The material of the holder is copper due to its high heat conductivity. The holder was cut at the Brewster incidence for ZnSe. When the crystal is put in the cavity at Brewster incidence, Fresnel losses (reflection losses) are minimized. The index of refraction (n_{ZnSe}) of ZnSe crystal is 2.45. The inverse tangent of n_{ZnSe} gives us the Brewster angle, which is 67.79^0. The angled part of the holder is for the crystal. The hole with a

diameter of $\varphi_3 = 3$ mm allows the passage of the pump light. The other hole in the left of the holder with a diameter of $\varphi_2 = 6.5$ mm is for the cold finger connection. Cold finger is also made of copper. Heat is transferred from the cold finger to the holder by surface contact, which is an effective method for copper.

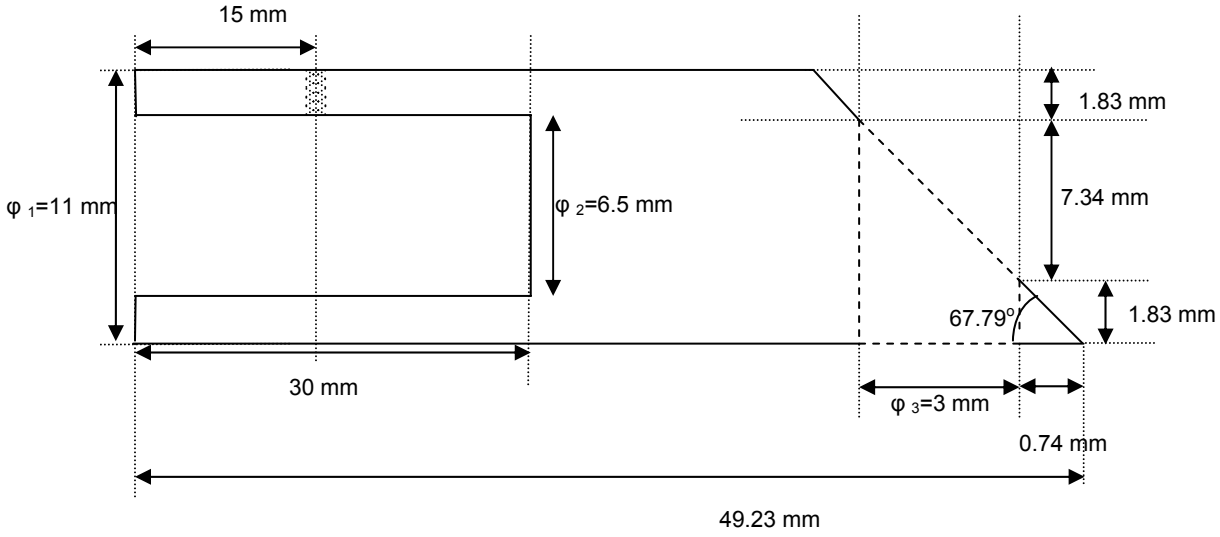

(a)

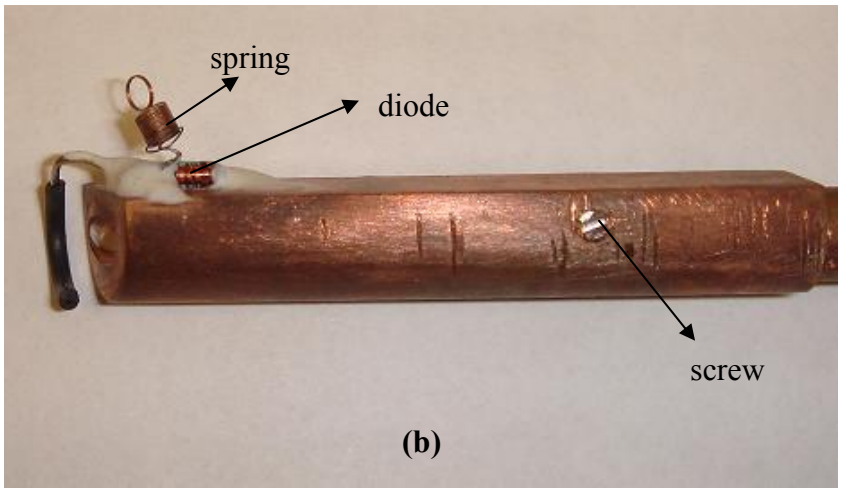

(b)

Figure 5.2: (a) Drawing and (b) photograph of the crystal holder. φ_1, φ_2, φ_3 are the diameters of the holder, the hole for cold finger, and the hole for the path of the light, respectively. Mounted diode and spring were used to measure the temperature.

In Figure 5.2 (b), the mounted diode and spring on the crystal holder are seen. With the diode and the spring, we can measure the temperature of the holder. More information about temperature measurements will be given later. Figure 5.3 shows the cold finger and the crystal holder part together. The crystal holder connection to the cold finger is established with a screw.

Figure 5.3: Picture of the cold finger and the crystal holder.

The end of the cold finger was connected to a thin, wide, copper wire. This part was put in the liquid nitrogen (LN) tank. A large part of this copper wire was isolated to minimize heat loss. The cold finger was connected to the vacuum chamber with a sealed glass. The drawings and the photograph of the vacuum chamber are shown in Figures 5.4. and 5.5. The shape of the vacuum chamber is cylindrical (dia: 40 mm), and it is made of stainless steal. It has three windows. Two of them are within the laser cavity while the third is for monitoring luminescence. Undoped polycrystalline ZnSe crystals (dia: 10 mm, thickness: 2 mm) were mounted on these windows with vacuum epoxy (Varian-Torr Seal Vacuum Epoxy). This is because pure ZnSe is transparent from 0.5 to 22 μm [21], which is appropriate to observe emission of the Fe^{2+}:ZnSe crystal. The laser cavity windows are also at Brewster incidence. The vacuum valve (Springless Diaphragm Valve-Swagelok) was also connected to the vacuum chamber with the stainless steel tube. Here, we used the valve in order to prevent the inside of the vacuum

chamber from moisture after the cooling process was finished. The vacuum valve was fastened to the vacuum pump. In our case, rough pumping was enough, so we did not use a high-vacuum pump. Figure 5.6 shows the whole system.

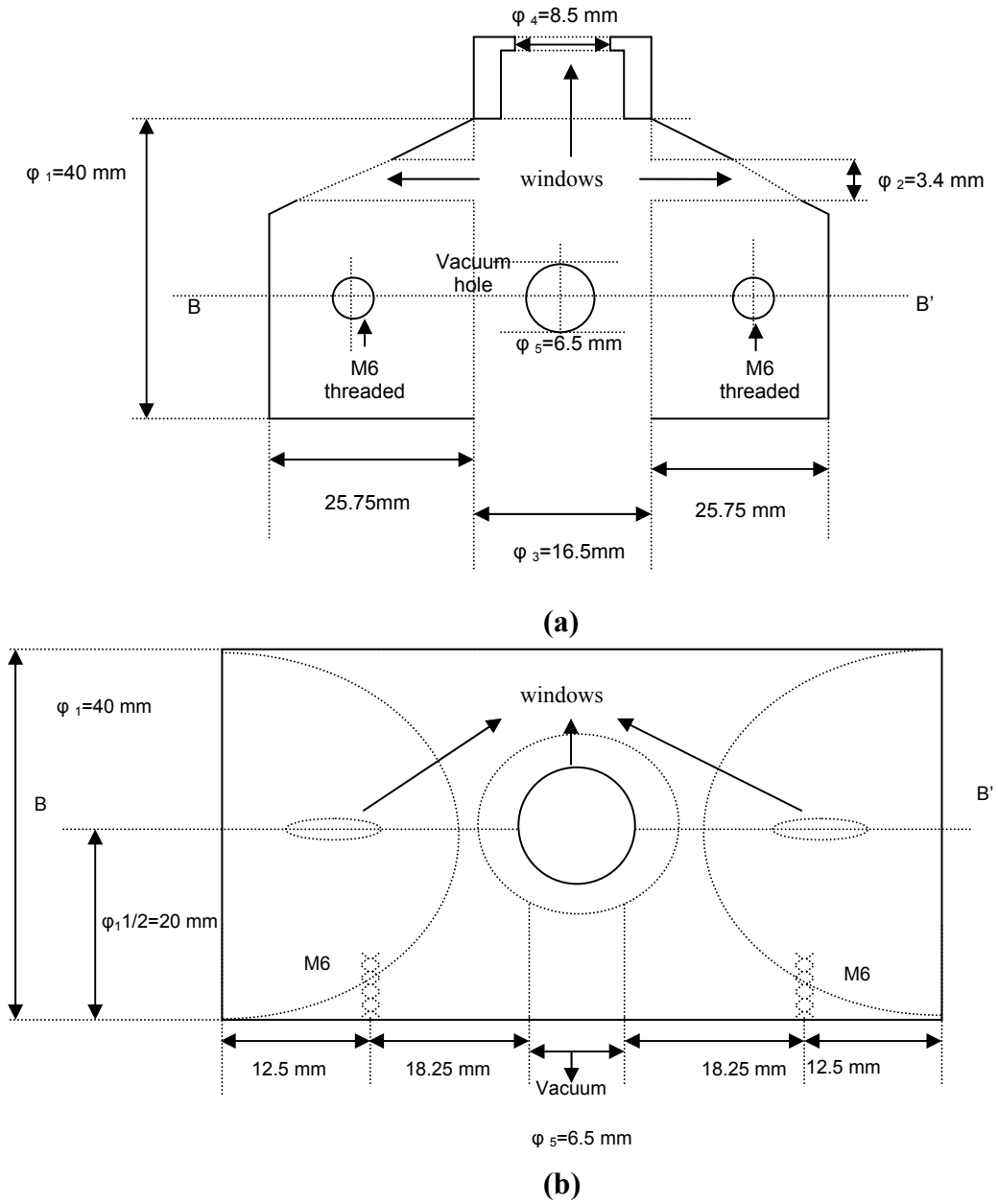

Figure 5.4: (a) Drawing of the vacuum chamber and (b) side view B-B[l] of drawing (a). φ_1, φ_2, φ_3, φ_4, φ_5 are the diameters of the vacuum chamber, laser cavity windows, hole for sealed glass that holds the cold finger, luminescence window, and vacuum hole, respectively. M6 threads are for posts. They are perpendicular to the optic axis.

Figure 5.5: Photograph of the vacuum chamber.

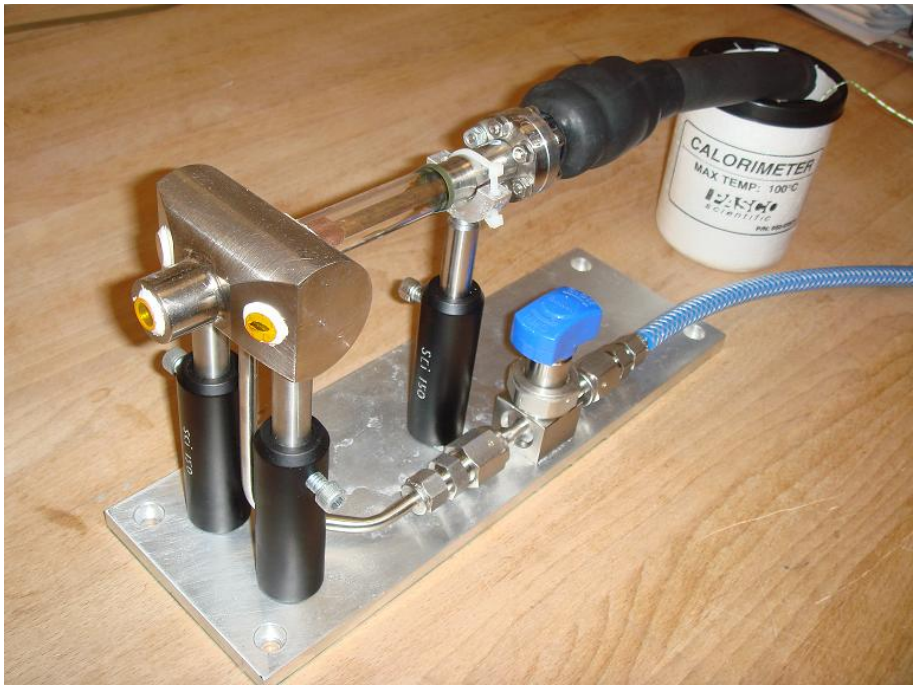

Figure 5.6: The whole cryogenic system.

The diode and the spring in Figure 5.2 were mounted on the crystal holder to measure the temperature of the crystal. The potential across the anode and the cathode of the diode changes with respect to the temperature. When the diode is cooled, the potential increases. At room temperature, the potential has a value of ≈ 0.6 V, while it is ≈ 1.04 V

at liquid nitrogen temperature (77 K). The cathode of the diode is connected to the crystal holder, in other words, the copper end of the cold finger. The anode of the diode is connected to the spring. The spring touches the surface of the vacuum chamber. Thus, we can measure the temperature as a difference in the voltage with a simple voltmeter. Figure 5.7 shows the calibrated temperature values as a function of the voltage across the diode.

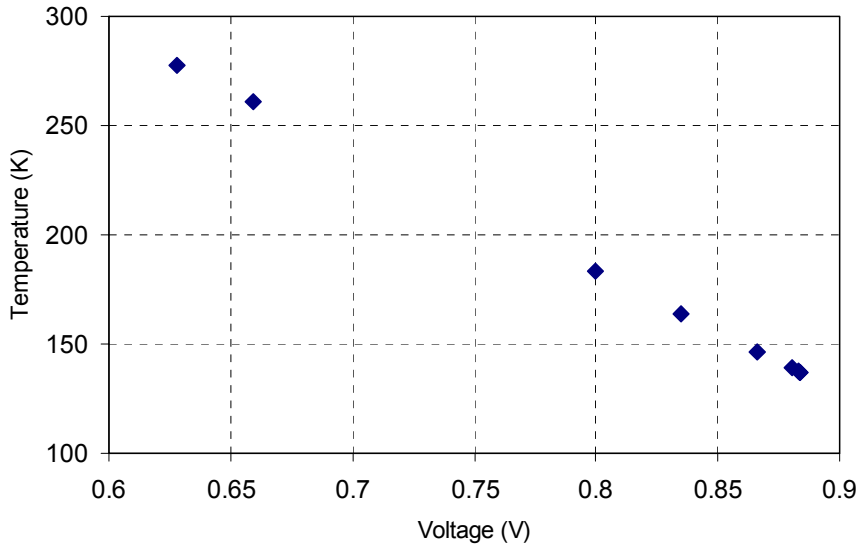

Figure 5.7: The calibrated temperature as a function of the potential difference across the diode.

We performed vacuum trials, after we completed the development of the cryogenic system. In vacuum systems, the vacuum pump is first started. After it reaches the stable value of vacuum, cooling is initiated. Subsequently, both the temperature and the pressure values of the system decrease. In the vacuum trials, we observed this expected trend in our system. Figure 5.8 shows the changes of pressure and temperature with respect to the pumping time. The system becomes stable approximately after 40 minutes of pumping with the roughing pump. The minimum obtained pressure value was measured to be 0.2 mbar at 137 K. According to reference [24], the luminescence lifetimes ranged from 5 to 105 μs for temperatures less than 220 K. Therefore, the obtained temperature value is sufficient for performing fluorescence measurements.

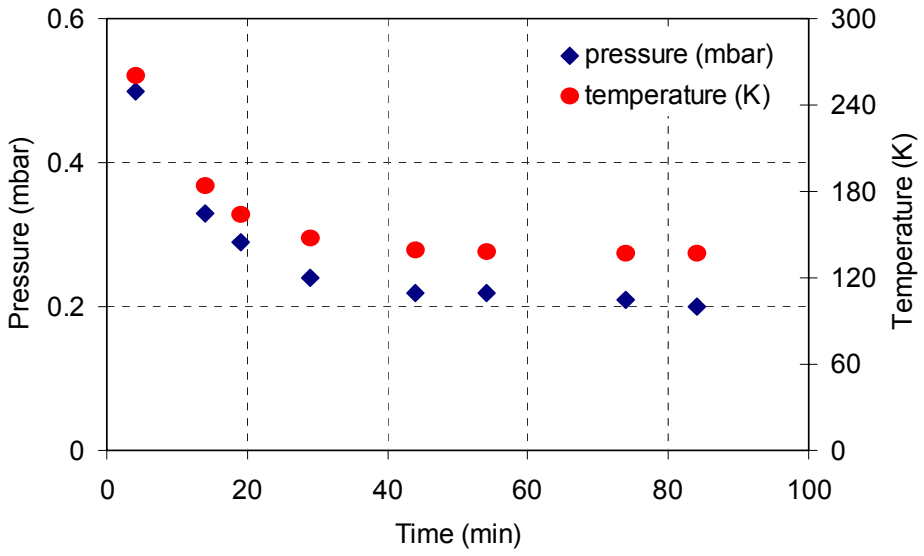

Figure 5.8: The changes in the pressure and temperature as a function of the pumping time.

However, in our system we were not able to adjust the temperature. The small changes on the pumping or the cooling rates influenced the temperature values. Therefore, we always had to work at the minimum possible temperature. After the successful vacuum trials, we used our cryogenic system in an attempt to make lifetime measurements

5.3 Trials of Lifetime Measurement and Lasing

Figure 5.9 shows the schematic of the lifetime measurements setup. In our experiments, the tunable Cr^{2+}:ZnSe laser operating at 2645 nm, and outputting 10-30 ns pulses was used as the pump source [52, 54]. The repetition rate was 1 kHz. The pump was focused inside the Fe^{2+}:ZnSe crystal with a 10-cm focal length CaF_2 lens (L1). Incident pump energy was around ≈ 42 µJ. Hamamatsu InSb and Electro Optical System Mercury Cadmium Telluride (MCT) liquid nitrogen cooled detectors were used during the experiments. The response of the first detector (Hamamatsu) is higher than that of the second (MCT) detector in the spectral range of 2-5 µm. However, after 5.2 µm, the first detector has a cut off, while the MCT detector can operate in the spectral range of 2-15

μm. We thought that Fe^{2+}:ZnSe might have luminescence band above the cut-off wavelength of the first detector. Therefore, we also tried the MCT detector. We used a filter in front of the detectors, which has high reflectivity at the pump wavelength, and high transmission at the expected emission wavelength of Fe^{2+}:ZnSe crystal. In order to collect the luminescence from the Fe^{2+}:ZnSe crystal, a MgF_2 lens (L2) with a focal length of 8 cm was located at 90^0 with respect to the direction of the excitation beam.

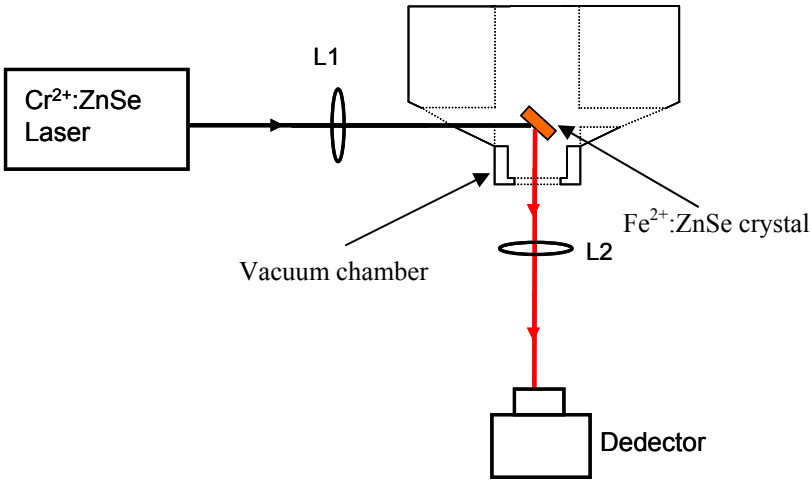

Figure 5.9: Schematic of the lifetime measurement setup. L1 is a CaF_2 lens with a focal length of 10 cm, L2 is a MgF_2 lens with a focal length of 8 cm. Cooled InSb or MCT detectors were used.

In the lifetime measurements, we used two different Fe^{2+}:ZnSe crystals. Table 5.1 shows the properties of the samples. Our cryogenic system was designed for samples with a diameter of ≈ 10 mm and thickness of ≈ 2 mm. Therefore, sample 1 (polycrystalline) was cooled in the experiments. Saturation analysis of sample 1 was also discussed in the previous chapter. The minimum temperature of 180 K was obtained during the lifetime measurements. According to reference [24], luminescence can be obtained below 220 K. However, we could not detect any luminescence signal. Then, we decided to try sample 2 (single crystal) at room temperature. We also could not observe any luminescence signal. The samples have higher absorption values at

longer wavelengths. The incident pump wavelength was tuned to a longer wavelength (2700 nm), and the trials were performed again with both crystals. Nevertheless, the luminescence of Fe^{2+}:ZnSe crystals could not be obtained at this wavelength.

sample no:	Diffusion Time (days)	Diffusion Temperature (C^0)	Crystal Length (mm)	$\alpha_{p0}(cm^{-1})$ at 2645 nm	Average Fe ion concentration (ion/cm^3)
1	4	1000	1.98	6.14	$6.8x10^{18}$
2	1.5	1000	0.7	5.64	$4.9x10^{18}$

Table 5.1: Properties of the Fe^{2+}:ZnSe crystals used in experiments.

The failure in the lifetime measurements affected the laser trials. If we had obtained luminescence signal, it would have been straightforward to align the laser cavity by maximizing the signal. In the laser trials, the 4-mirror Fe^{2+}:ZnSe laser x-cavity was set up. Figures 5.10 and 5.11 show the schematic and photograph of the experimental setup.

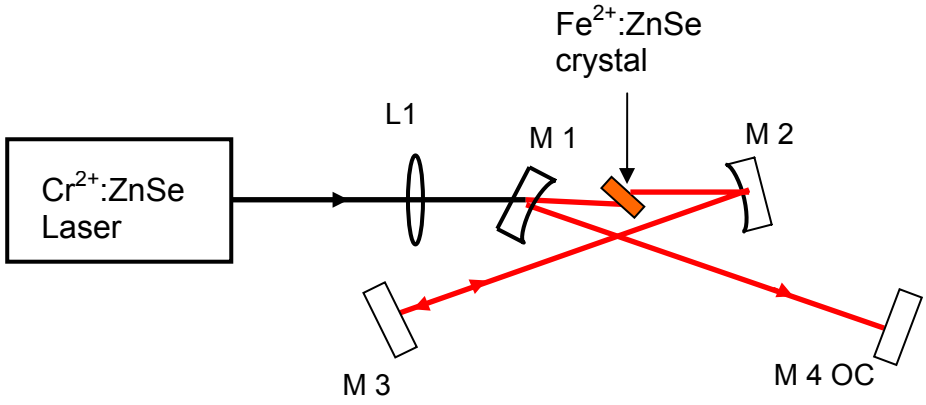

Figure 5.10: 4-mirror Fe^{2+}:ZnSe laser cavity. L1 is the lens with a focal length of 10 cm. M1 and M2 are concave mirrors. They are highly reflective at 4300 nm with a radius of curvature 10 cm. M3 is the flat mirror highly reflective at 4300 nm. M4 is the flat output coupler with %10 transmission at 4300 nm.

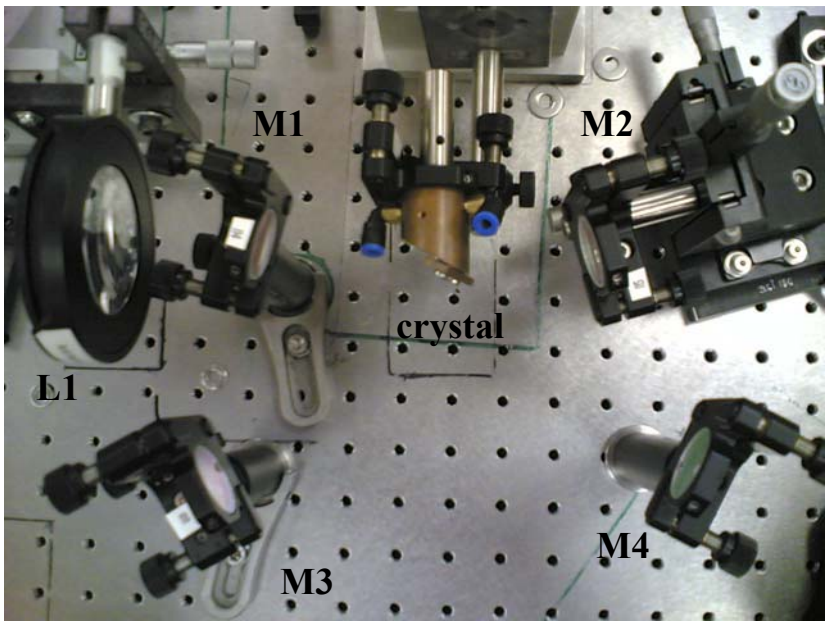

Figure 5.11: Photograph of the 4-mirror Fe^{2+}:ZnSe laser cavity.

The Cr^{2+}:ZnSe laser operating at 2645 nm was focused inside the crystal with a CaF_2 lens (L1) having a focal length of 10 cm. Two identical concave mirrors (M1 and M2) highly reflective at 4300 nm with a radius of curvature 10 cm were around the crystal. A flat mirror (M3), highly reflective at 4300 nm was put in the feedback arm. A flat output coupler (M4) with 10% transmission at 4300 nm was further used. All mirror substrates were made of CaF_2. The designed x-cavity laser system has two important advantages. First, in order to tune the laser output wavelength, a prism can be put into the cavity, between the mirrors M2 and M3. Second, the spot-size of the pump source can be made smaller by using x-cavity design, in comparison with a 2-mirror resonator.

The lifetime measurements were tried with the two crystals at low and room temperature. In both measurements we could not observe any signal. The single crystal sample could not be placed inside the cryogenic system due to its size. Therefore, the single-crystal was not cooled (sample 2). In addition, we could not observe the minimum temperature (137 K) in the trials, due to the heat load covered by the pump laser source. We were able to reduce the temperature up to 180 K. The cooling mechanism can be improved by using high vacuum systems. It is likely that sample 2

will produce fluorescence when cooled. However, this was not tried. In these experiments, we had a limited number of samples. Furthermore, the pump sources used in the literature are generally operating around 3 μm [25-28]. The output power of our pump source decreases when we select longer wavelengths. We believe that by further improving the sample quality, cooling scheme and by using longer-wavelength pump source, it should be possible to observe fluorescence and lasing from Fe^{2+}:ZnSe.

Chapter 6

Conclusions

In this thesis, we have presented the spectroscopic investigation of CdS quantum dots and Fe^{2+}:ZnSe crystals. The review and theoretical analysis of quantum dots including the effective-mass approximation method were first discussed. Brus equation was analyzed and used in the determination of the size of nanoparticles. We have provided the first detailed information about the spectroscopic properties of PAA coated CdS quantum dots [11]. Characterization of CdS quantum dots including the determination of crystal size, photoluminescence intensity, and quantum yield was investigated. The results show that there is a critical COOH/Cd ratio (1.5-2) in order to obtain the highest PL intensity, quantum yield, and smaller crystal sizes. The effect of reaction pH was also investigated. CdS nanoparticles prepared at pH 7.5 have higher quantum yields than those prepared at 5.5.

Saturation analysis of Fe^{2+}:ZnSe crystals was then discussed. The experiments were performed at two different wavelengths (2645 and 2730 nm) with two different methods. The absorption cross section (σ_a) and normalized strength of excited-state absorption (f_p) were determined. The results are comparable within each method. We have attempted to make lifetime measurements and laser trials with polycrystalline and single-crystal Fe^{2+}:ZnSe samples at low and room temperature. For low-temperature measurements, a cryogenic system was designed and developed that enables cooling down to 136 K. Under heat loading, the minimum temperature obtained was 180 K. We could not obtain any signal during the lifetime measurements. The failure in the lifetime measurements affected the laser trials. The amount of Fe ion concentration, the limited output power of the pump source, limited cooling and the defects on the crystal surface are possible reasons for the failure in the experiments. In order to obtain luminescence

and laser emission from Fe^{2+}:ZnSe crystal, new samples can be synthesized and tried with an improved pump source and more aggressive cooling mechanism.

BIBLIOGRAPHY

[1] Alivisatos, A.P., *Perspectives on the physical chemistry of semiconductor nanocrystals.* Journal of Physical Chemistry, 1996. **100**(31): p. 13226-13239.

[2] Brus, L.E., *Electron-electron and electron-hole interactions in small semiconductor crystallites: The size dependence of the lowest excited electronic state.* J. Chem. Phys., 1984. **80**(9): p. 4403-4409.

[3] Ozkan, M., *Quantum dots and other nanopartciles: what can they offer to drug discovery?* Drug Discovery Today, 2004. **9**(24): p. 1065-1071.

[4] Marti, A., et al., *Novel Semiconductor solar cell structures: The quantum dot intermediate band solar cell.* Thin Solid Films, 2006. **511-512**: p. 638-644.

[5] Landi, B.J., et al., *CdSe quantum dot-single wall carbon nanotube complexes for polymeric solar cells.* Solar Energy Materials & Solar Cells, 2005. **87**: p. 733-746.

[6] Weng, J.F., et al., *Highly luminescent CdTe quantum dots prepared in aqueous phase as an alternative fluorescent probe for cell imaging.* Talanta, 2006. **70**(2): p. 397-402.

[7] Henini, M. and M. Bugajski, *Advances in self-assembled semiconductor quantum dot lasers.* Microelectronics Journal, 2005. **36**(11): p. 950-956.

[8] Trindade, T., P. O'Brien, and N.L. Pickett, *Nanocrystalline Semiconductors: Synthesis, Properties, and Perspectives.* Chemical Materials, 2001. **13**: p. 3843-3858.

[9] Yin, Y. and A.P. Alivisatos, *Colloidal nanocrystal synthesis and the organic-inorganic interface.* Nature, 2005. **437**(7059): p. 664-670.

[10] Spanhel, L., et al., *Photochemistry of Colloidal Semiconductors .20. Surface Modification and Stability of Strong Luminescing Cds Particles.* Journal of the American Chemical Society, 1987. **109**(19): p. 5649-5655.

[11] Celebi, S., et al., *Synthesis and Characterization of Poly(acrylic acid) Stabilized CdS Quantum Dots.* J. Phys. Chem. B (submitted), 2007.

[12] Sorokin, E., S. Naumov, and I.T. Sorokina, *Ultrabroadband infrared solid-state lasers.* Ieee Journal of Selected Topics in Quantum Electronics, 2005. **11**(3): p. 690-712.

[13] Adams, J.J., et al. *Tunable laser action at 4.0 microns from Fe:ZnSe*. in *Advanced Solid State Lasers*. 1999. Boston: OSA.

[14] Slack, G.A., F.S. Ham, and R.M. Cherenko, *Optical Absorption of Tetrahedral Fe^{2+} (cd^6) in Cubic ZnS, CdTe, and $MgAl_2O_4$.* Physical Review, 1966. **152**(1): p. 376-402.

[15] Slack, G.A. and B.M. Omera, *Infrared Luminescence of Fe^{2+} in ZnS.* Physical Review, 1967. **163**(2): p. 335-341.

[16] Slack, G.A., S. Roberts, and F.S. Ham, *Far-Infrared Optical Absorption of Fe^{2+}: in ZnS.* Physical Review, 1967. **155**(2): p. 170-177.

[17] Vallin, J.T., et al., *Infrared Absorption in Some II-VI Compounds Doped with Cr.* Physical Review B, 1970. **2**(11): p. 4313-4333.

[18] Grebe, G., G. Roussos, and H.-J. Schulz, *Infrared luminescence of ZnSe:Cr crystals.* Journal of Luminescence, 1976. **12-13**: p. 701-705.

[19] DeLoach, L.D., et al., *Transition Metal-Doped Zinc Chalcogenides Spectroscopy and Laser Demonstration of a New Class of Gain Media.* IEEE Journal of Quantum Electronics, 1996. **32**(6): p. 885-895.

[20] Page, R.H., et al., *Cr^{2+} Doped Zinc Chalcogenides as Efficient, Widely Tunable Mid-Infrared Lasers.* IEEE Journal of Quantum Electronics, 1997. **33**(4): p. 609-619.

[21] Gavrushchuk, E.M., *Polycrystalline zinc selenide for IR optical applications.* Inorganic Materials, 2003. **39**(9): p. 883-898.

[22] Adachi, S. and T. Taguchi, *Optical Properties of ZnSe.* Physical Review B, 1991. **43**(12): p. 9569-9577.

[23] Demirbas, U., A. Sennaroglu, and M. Somer, *Sythesis and characterization of diffusion-doped Cr^{2+}:ZnSe and Fe^{2+}:ZnSe.* Optical Materials, 2006. **28**: p. 231-240.

[24] Adams, J.J., et al., *4.0-4.5 mm lasing of Fe: ZnSe below 180 K, a new mid-infrared laser material.* Optics Letters, 1999. **24**(23): p. 1720-1722.

[25] Akimov, V.A., et al., *Efficient IR Fe : ZnSe laser continuously tunable in the spectral range from 3.77 to 4.40 ttm.* Quantum Electronics, 2004. **34**(10): p. 912-914.

[26] Voronov, A.A., et al., *Laser parameters of a Fe:ZnSe crystal in the 85-255-K temperature range.* Quantum Electronics, 2005. **35**(9): p. 809-812.

[27] Kernal, J., et al., *3.9-4.8 mm gain-switched lasing of Fe:ZnSe at room temperature.* Optics Express, 2005. **13**(26): p. 10608-10615.

[28] Fedorov, V.V., et al., *3.77-5.05-mm tunable solid-state lasers based on Fe2+-doped ZnSe crystals operating at low and room temperatures.* IEEE Journal of Quantum Electronics, 2006. **42**(9-10): p. 907-917.

[29] Voronov, A.A., et al., *Passive Fe^{2+}:ZnSe single-crystal Q switch for 3-mm lasers.* Quantum Electronics, 2006. **36**(1): p. 1-2.

[30] Kisel, V.E., et al., *Saturable Absorbers for Passive Q-Switching of Erbium Lasers Emitting in the Region of 3 um.* Journal of Applied Spectroscopy, 2005. **72**(6): p. 818-823.

[31] Jacak, L., P. Hawrylak, and A. Wojs, *Quantum Dots*. 1998: Springer.

[32] Pejova, B. and I. Grozdanov, *Three-dimensional confinement effects in semiconducting zinc selenide quantum dots deposited in thin-film form.* Materials Chemistry and Physics, 2005. **90**(1): p. 35-46.

[33] Harrison, P., *Quantum Wells, Wires and Dots*. 2005: Wiley.

[34] Trindade, T., P. OBrien, and X.M. Zhang, *Synthesis of CdS and CdSe nanocrystallites using a novel single-molecule precursors approach.* Chemistry of Materials, 1997. **9**(2): p. 523-530.

[35] Banyai, L. and S.W. Koch, *Semiconductor Quantum Dots*. 1993: World Scientific.

[36] Griffiths, D.J., *Introduction to Quantum Mechanics*. 1995: Prentice-Hall.

[37] Liboff, R.L., *Introductory Quantum Mechanics*. 4 ed. 2003: Addison Wesley.

[38] Nosaka, Y., *Finite Depth Spherical Well Model for Excited-States of Ultrasmall Semiconductor Particles - an Application.* Journal of Physical Chemistry, 1991. **95**(13): p. 5054-5058.

[39] Pellegrini, G., G. Mattei, and P. Mazzoldi, *Finite depth square well model: Applicability and limitations.* Journal of Applied Physics, 2005. **97**(7): p. -.

[40] Brus, L.E., *A simple model for the ionization potential, electron affinity, and aqueous redox potentials of small semiconductor crystallites.* Journal of Chemical Physics, 1983. **79**(11): p. 5566-5571.

[41] Burda, C., et al., *Chemistry and Properties of Nanocrystals of Different Shapes.* Chem. Rev., 2005. **105**: p. 1025-1102.

[42] Brus, L., *Electronic Wave Functions in Semiconductor Clusters: Experiment and Theory.* Journal of Physical Chemistry, 1986. **90**: p. 2555-2560.

[43] Raji, P., C. Sanjeeviraja, and K. Ramachandran, *Thermal properties of nano crystalline CdS.* Crystal Research and Technology, 2004. **39**(7): p. 617-622.

[44] Castanon, G.A.M., et al., *Synthesis of CdS Nanoparticles: a Simple Method in Aqueous Media.* Advances in Technology of Materials and Materials Processing, 2005. **7**(2): p. 171-174.

[45] Celebi, S., *M.S. Thesis.* 2007.

[46] Sondi, I., O. Siiman, and E. Matijevic, *Synthesis of CdSe nanoparticles in the presence of aminodextran as stabilizing and capping agent.* Journal of Colloid and Interface Science, 2004. **275**: p. 503-507.

[47] Wuister, S.F. and A. Meijerink, *Synthesis and luminescence of (3-mercaptopropyl)- trimethoxysilane capped CdS quantum dots.* Journal of Luminescence, 2003. **102-103**: p. 338-343.

[48] Reiss, P., et al., *Low polydispersity core/shell nanocrystals of CdSe/ZnSe and CdSe/ZnSe/ZnS type: preparation and optical studies.* Synthetic Metals, 2003. **139**(3): p. 649-652.

[49] Hines, M.A. and P. Guyot-Sionnest, *Synthesis and characterization of strongly luminescing ZnS-Capped CdSe nanocrystals.* Journal of Physical Chemistry, 1996. **100**(2): p. 468-471.

[50] Gerion, D., et al., *Synthesis and properties of biocompatible water-soluble silica-coated CdSe/ZnS semiconductor quantum dots.* Journal of Physical Chemistry B, 2001. **105**(37): p. 8861-8871.

[51] Sennaroglu, A., et al., *Accurate determination of saturation parameters for Cr^{4+}-doped solid-state saturable absorbers.* Journal of Optical Society of America B, 2006. **23**(2): p. 241.

[52] Demirbas, U. and A. Sennaroglu, *Intracavity-pumped Cr^{2+}: ZnSe laser with ultrabroad tuning range between 1880 and 3100 nm.* Optics Letters, 2006. **31**(15): p. 2293-2295.

[53] Kück, S., *Laser-related spectroscopy of ion-doped crystals for tunable solid-state lasers.* Applied Physics B, 2001. **72**: p. 515-562.

[54] Sennaroglu, A., et al., *Concentration dependence of fluorescence and lasing efficiency in Cr^{2+} : ZnSe lasers.* Optical Materials, 2007. **29**(6): p. 703-708.

VITA

Ahmet Koray Erdamar was born in Ankara, Turkey, on June 3 1982. He received his BS degree in Physics from Middle East Technical University (METU), Ankara in June 2005. He was accepted to Department of Physics MS program at Koç University (KU), Istanbul in August 2005. He worked at KU as a research and teaching assistant until August 2007. His research interests include spectroscopic investigation of novel luminescent materials. He will continue his Ph.D. work in Micro and Nanotechnology program at METU.

List of Publications:

Serdar Celebi, Ahmet Koray Erdamar, Alphan Sennaroglu, Adnan Kurt, and Havva Yagci Acar, "Synthesis and Characterization of Poly(acrylic acid) Stabilized CdS Quantum Dots", Journal of Physical Chemistry B, Submitted, 2007.